Published in final edited form as:
IEEE Trans Med Imaging. 2010 November ; 29(11): 1821–1838. doi:10.1109/TMI.2010.2050779.

Volumetric Topological Analysis: A Novel Approach for Trabecular Bone Classification on the Continuum between Plates and Rods

Punam K Saha[1,*], **Yan Xu**[1], **Hong Duan**[1], **Anneliese Heiner**[2], and **Guoyuan Liang**[1]

[1] Departments of Electrical and Computer Engineering and Radiology, University of Iowa, Iowa City, IA 52242

[2] Departments of Orthopaedics and Rehabilitation and Biomedical Engineering, University of Iowa, Iowa City, IA 52242

Abstract

Trabecular bone (*TB*) is a complex quasi-random network of interconnected plates and rods. TB constantly remodels to adapt to the stresses to which it is subjected (Wolff s Law). In osteoporosis, this dynamic equilibrium between bone formation and resorption is perturbed, leading to bone loss and structural deterioration, both increasing fracture risk. Bone s mechanical behavior can only be partially explained by variations in bone mineral density, which led to the notion of bone structural quality. Previously, we developed digital topological analysis (*DTA*) which classifies plates, rods, profiles, edges, and junctions in a TB skeletal representation. Although the method has become quite popular, a major limitation of DTA is that it provides only hard classifications of different topological entities, failing to distinguish between narrow and wide plates. Here, we present a new method called volumetric topological analysis (*VTA*) for regional quantification of TB topology. At each TB location, the method uniquely classifies its topology on the continuum between perfect plates and perfect rods, facilitating early detections of TB alterations from plates to rods according to the known etiology of osteoporotic bone loss. Several new ideas, including manifold distance transform, manifold scale, and feature propagation have been introduced here and combined with existing DTA and distance transform methods, leading to the new VTA technology. This method has been applied to multi-detector CT and μCT images of four cadaveric distal tibia and five distal radius specimens. Both intra- and inter-modality reproducibility of the method has been examined using repeat CT and μCT scans of distal tibia specimens. Also, the method s ability to predict experimental biomechanical properties of TB via CT imaging under *in vivo* conditions has been quantitatively examined and the results found are very encouraging.

Keywords

Trabecular bone; skeletonization; quantitative topology; digital topological analysis; distance transform; manifold distance transform; manifold scale; CT imaging; experimental biomechanics

1 INTRODUCTION

Trabecular bone (*TB*) is a complex quasi-random network of interconnected plates and rods. In human skeletons, trabeculae are typically 100–200 μm thick [1]. TB constantly remodels through a complex interplay between bone formation by osteoblasts and bone resorption by osteoclasts to adapt dynamically to the stresses to which it is subjected (Wolff s Law [2]). In

[*]Corresponding author: pksaha@engineering.uiowa.edu Telephone: (319) 335-6420.

osteoporosis, this dynamic equilibrium between bone formation and resorption is perturbed, leading to bone loss and structural deterioration. Both bone loss and structural deterioration increase fracture risk and most osteoporotic fractures occur at sites rich in TB. Approximately, 30% of postmenopausal white women in the United States suffer from osteoporosis [3] and the prevalence in Europe and Asia is similar. In the United States alone, 10 million individuals are estimated to have osteoporosis and almost 34 million more may have low bone mass, a condition called “osteopenia”, placing the latter at high risk of developing the disease [4]. The clinical manifestations of osteoporosis are fractures of the vertebrae, upper femur, humerus and wrist. The continued rise in life expectancy is predicted to result in large increase in fracture incidence in the current century [5].

Although the clinical definition of osteoporosis refers to a condition in which bone mineral density (*BMD*) is at least 2.5 standard deviations below the mean of the young adult population [6], bone s mechanical competence can only be partially explained by variations in BMD. Recently, it has been shown that, on the average, BMD explains about 60% of bone strength as estimated from a meta analysis of 38 studies investigating some measures of bone strength [7]. These observations led to the notion of bone quality, chief among which is architecture as a determinant of TB strength. Based on a study involving postmenopausal women, Kleerekoper *et al.* [8] found that subjects with osteoporotic vertebral compression deformities, had a significantly lower mean TB plate density as compared to an age and BMD matched control group of subjects without fractures. In a study involving 69 postmenopausal women with 37 women suffering and 32 women without fractures, Moore *et al.* [9] reported inter-trabecular spacing to be a more significant differentiator than BMD. Recker [10] observed decreased TB plate density and increased marrow star volume [11] for a group of patients with vertebral crush fractures as compared to another group consisting of equal number of BMD-matched controls. There are several other clinical studies [12–16] supporting the notion of TB architectural quality.

The conventional tool for assessing TB structure is histomorphometry from bone biopsies [17–18]. Since histomorphometric approaches are primarily based on two-dimensional (*2D*) cross-sections, in recent years, the method has been superseded by direct three-dimensional (*3D*) analysis of biopsy specimens imaged by micro-computed tomography (μCT) [19]. μCT instruments have maximum resolution of the order of 8 μm isotropic voxels providing detailed insight into TB microarchitecture. Although the method is nondestructive, it is invasive, since bone biopsies are required for μCT imaging which is rarely indicated clinically and not suited for following patients longitudinally to evaluate treatment response. More recently, the μCT cone-beam scanning technology has been incorporated into dedicated CT systems designed for high-resolution imaging of TB at the distal extremities, i.e. the distal radius and tibia [20–21]. The rapid diffusion of multi-detector CT systems also opens opportunities for TB structure analysis in the axial skeleton or distal extremities [22–26]. Saha *et al.* [24] reported reproducibility of multi-detector CT derived structural and topological measures of TB in cadaveric ankle and also studied the correlation between TB measures derived via multi-detector CT and μCT imaging. Bredella *et al.* [25] studied effectiveness of flat-panel volume CT derived TB structural parameters in predicting anorexia nervosa in adolescent girls. They observed bone structural abnormality in patients as compared with age and sex-matched normal-weight control subjects. Recently, Diederichs *et al.* [26] has studied the correlation of between TB parameters derived via multi-detector CT and μCT imaging of cadaveric ankles and has also investigated the ability of CT derived parameters to predict bone mechanical strength. Remarkable progress in high-resolution MRI during the past 10 years now offers a new tool for TB structure assessment (for pertinent reviews, see [7, 27–30]). A review of advanced imaging of bone macro and micro structure has been reported by Genant *et al.* [31]. In a comparative study between TB structural parameters obtained from high-resolution MR and multi-detector CT, Link *et al.* [32] observed a high correlation between MR- and CT-

derived structural parameters and those derived from contact radiographs. Although, recent advances in CT and MRI allow imaging of TB *in vivo*, the limited SNR precludes voxel sizes much smaller than TB thickness (100–200μm), therefore resulting in images that are inherently fuzzy. Most conventional histomorphometric approaches to TB structural assessment are not effective at *in vivo* resolution regime.

Various topologic and geometric approaches to characterize TB architecture have been reported in literature [33–45]. Parfitt *et al.* [33] conceived a parallel interconnected plate model of TB yielding bone area fraction, TB volume fraction, TB spacing, and TB number from 2D histomorphometric sections. Vesterby *et al.* [34] conceived a new stereologic parameter, called star volume, which is the average volume of an object region that can be seen from a point inside that region un-obscured in all directions. Hahn *et al.* [35] introduced the "trabecular bone pattern factor" which captures TB connectivity in terms of convexity property of TB surface defined as ratio of the differences in perimeter and area under dilation. Hildebrand *et al.* [36] developed a 3D structure model index, a function of global plate-to-rod ratio, based on the observation that the rate of change of volume with thickness for a plate is different from that for a rod. Majumdar *et al.* [37] have adopted apparent TB number, apparent TB thickness, apparent TB spacing and fractal dimension to quantify TB structural quality. Stampa *et al.* [38] introduced two new measures, namely, relative plate and relative rod volume using TB voxel counts in 3 × 3 planes around each TB voxel. Some investigators [39–40] have analyzed the nodes and free ends of TB. Feldkamp *et al.* [41] showed that the makeup of TB networks can be expressed in terms of topological entities such as the 3D Euler number. Saha *et al.* [42] introduced the notion of characterizing plat-like and rod-like geometry of a local structure by analyzing structural anisotropy using tensor scale [46–47]. Recently, Vasili *et al.* [43] has presented a method of characterizing rod-like and plate-like structures in a TB network using inertial anisotropy. Bonnassie *et al.* [44] presented a new method of characterizing local shape using medial axis transformation. Carballido-Gamio *et al.* [45] has developed a new method of analyzing TB structure by analyzing structural anisotropy at junctions on 2D image-slices.

Previously, we developed digital topological analysis [48–50] which classifies plates, rods, profiles, junctions, and edges in a skeletal representation of a TB network. Although, the method is being widely used for quantification of TB structural quality, a major limitation of the method is that resulting classifications are inherently binary failing to distinguish between narrow and wide plates. Here, we introduce a new method called volumetric topological analysis for regional quantification of TB topology. At each TB location, the method uniquely classifies topology of the local trabecula on the continuum between perfect plates and rods facilitating early detections of TB alterations from plates to rods according to the known etiology of osteoporotic bone loss.

2 THEORY AND ALGORITHMS

A previously published digital topological analysis (*DTA*) method [48–50] successfully identifies different topological entities (Figure 1(a)) in a surface skeletal representation of a TB network. However, it suffers from two major limitations – (1) binary classification of plates and rods and (2) failure to obtain topological characterization in a volumetric representation. The proposed volumetric topological analysis (*VTA*) method is aimed to overcome these two limitations. VTA identifies topological entities on the continuum between perfect plates and perfect rods in a volumetric representation of a quasi-random mesh-like structure including TB networks (Figure 1(b)). Also, it may be applicable to simpler structures, often used in robotic 3D object recognition [51]. VTA is accomplished using the following sequential steps – (1) surface skeletonization [52–56], (2) digital topological analysis [48–49], (3) manifold distance transform (*MDT*), (4) manifold scale computation, and (5) volumetric feature propagation. The results of intermediate steps in VTA are illustrated in Figure 2. The first two

steps are accomplished using our previously reported algorithms except that the output of surface skeletonization is further improved using a new noise pruning algorithm described in Section 2.4. In the rest of this paper, by skeletonization , we will understand surface skeletonization unless stated otherwise. Several new concepts and algorithms including manifold distance transform and manifold scale are introduced in this paper. Feature propagation technique was previously presented by Bonnassie *et al.* [44]. Here, we propose a scan-independent solution to the problem.

First, we schematically describe the measure we intend to compute using the new algorithm. Let us consider a surface-like volume object and its skeleton as shown in Figure 3. As illustrated in the figure local structure thickness and width are two independent measures. Local structure thickness may be computed by sampling binary or fuzzy distance transform along skeletal locations [57–58]. However, to compute local skeletal width (see Figure 3), we need a technique similar to manifold distance transform (see Section 2.3). Following the description in the figure, a manifold distance transform from skeletal surface edge only provides local skeletal width. During a skeletonization process, a volume object is peeled by one voxel per iteration leading to a difference in width between the volume object and its skeleton (see Figure 3). Moreover, this difference is related to structure thickness at skeletal edges. Therefore, it is necessary to initialize manifold distance transform at skeletal edges by local thickness to compute the thickness of actual volumetric object (see Section 2.3). Essentially, VTA is designed to compute local width of a volume object which is subsequently used to classify individual trabecula on the continuum between a perfect plate and a perfect rod. In following sections, we describe the theory and algorithms for different steps involved in VTA starting with common definitions and notations used throughout the paper.

2.1 Definitions and Notations

In this paper, we use $\mathbb{R}$ to denote the set of real numbers while $\mathbb{Z}$ is used to denote the set of integers. It may be noted that $\mathbb{R}^3$ denotes the continuous 3D-space. We use $\mathbb{Z}^3$ to represent a *digital space* and each element of a digital space is referred to as a *voxel* whose position is denoted by Cartesian coordinates $(x_1, x_2, x_3)| x_1, x_2, x_3 \in \mathbb{Z}$. For any two voxels $p, q \in \mathbb{Z}^3$, |p–q| denotes the Euclidean distance between the two voxels. Although, the theory and methods immediately extend to fuzzy objects, the current development of VTA is confined to binary digital images, i.e., a voxel may have only two values – object and background. Such images are often obtained by thresholding [59–60] a gray-scale intensity image into object and background regions. An *object* in a binary image may be represented as a set $O \subset \mathbb{Z}^3$ of voxels. Following the fact that the field of view of an acquired image is always finite, the cardinality of an object O, denoted by $\| O \|$, is always finite. We use $\bar{O} = \mathbb{Z}^3 - O$ to denote the background for the object O. In the current application, the set of bone voxels constitutes the object and the background represents the set of all marrow or other non-trabecular bone voxels. Two voxels $(x_1, x_2, x_3)$and (y_1, y_2, y_3) are called *6-adjacent* if and only if $\sum_{i=1}^{3}(x_i - y_i)^2 \leq 1$ (face adjacent only); they are called *18-adjacent* if and only if $\sum_{i=1}^{3}(x_i - y_i)^2 \leq 2$ (face or edge adjacent); and they are called *26-adjacent* if and only if $\sum_{i=1}^{3}(x_i - y_i)^2 \leq 3$ (face, edge, or corner adjacent). Two α-adjacent voxels, where $\alpha \in \{6,18,26\}$, are often referred to as α-*neighbors* of each other. Let $p = (x_1, x_2, x_3)$ denote a voxel and let $q = (y_1, y_2, y_3)$ and $r = (z_1, z_2, z_3)$ denote two 6-neighbors of p. The two voxels q, r are referred to as *opposite 6-neighbor*s of p if and only if $y_i – x_i = x_i – z_i = \pm 1$, for some $i \in \{1,2,3\}$; note that the two opposite 6-neighbors q, r share two opposite faces of the voxel p. To satisfy the Jordan surface property in a binary digital image, whenever 26-adjacency is used for object (i.e., the set of bone voxels), 6-adjacency must be used for the background (i.e., the set of marrow or other non-trabecular bone voxels) and vice versa [61]. It ensures that a closed object surface is the necessary and

sufficient condition to separate the background into two components – the interior and the exterior. Here, we use 26-adjacency for object voxels and 6-adjacency for background voxels. Often, a topological property derived with such an adjacency convention is referred to as a (26,6) topological property.

In digital topology, we often refer to three entities – components, tunnels, and cavities; we define these three entities in the following. Let S be a nonempty set of voxels. An α-*path*|$\alpha \in \{6,18,26\}$ in S between two voxels $p, q \in S$ is a sequence of voxels $\langle p = p_0, p_1, \ldots, p_n = q \rangle$ in S such that p_i is α-adjacent to p_{i+1} for all $0 \leq i < n$. An α*-curve* is an α-path $\langle p_0, p_1, \ldots, p_n \rangle$ if and only if p_i, for $0 < i\ n$, has exactly two α-neighbors on the path. An α-path (or, an α-curve) is an α*-closed path* (respectively, an α*-closed curve*) if p_0 is α-adjacent to p_n. Two voxels $p, q \in S$ are α*-connected* in S if there exists an α-path from p to q in S. An α*-component* of S is a maximal subset of S where each pair of voxels is α-connected in S. A *cavity in S* is a 6-component of $\bar{S}$ surrounded by S. Although tunnels are easily visualized and intuitively described, they are difficult to formally define. However, the number of tunnels in an object can be defined precisely. Intuitively, a tunnel is formed by bending a cylinder to connect its two ends to each other or to a single connected object, e.g., the handle of a coffee mug. More accurately, the number of tunnels in an object is the rank of its first homology group [62].

In the following discussions, for any voxel p, $\mathcal{N}(p)$ denotes the set of all voxels in the $3 \times 3 \times 3$ neighborhood of p including p and $\mathcal{N}^*(p)$ denotes the set $\mathcal{N}(p) - \{p\}$. Because of the structure of $3 \times 3 \times 3$ neighborhood, assuming that the central voxel p is an object voxel, the set of all object voxels in $\mathcal{N}(p)$ always forms exactly one 26-connected component without tunnels and cavities [63], i.e., the topological property of the set of object voxels in $\mathcal{N}(p)$ is invariant. Therefore, the local topology of a voxel p is solely characterized by the set of object voxels in $\mathcal{N}^*(p)$. Let $\xi(p)$, $\eta(p)$ and $\delta(p)$, respectively, denote the numbers of object components, tunnels, and cavities formed by the set of object voxels in $\mathcal{N}^*(p)$. The entities $\xi(p)$, $\eta(p)$, and $\delta(p)$ are referred to as *local topological parameter*s of p [48–49]. Let $X(p)$ and $Y(p)$ denote the sets of 6- and 18-adjacent background neighbors of p, respectively. The following two theorems [48, 64–65] provide computational definitions of $\eta(p)$ and $\delta(p)$:

Theorem 1—If $X(p)$ is nonempty, the number of tunnels $\eta(p)$ is one less than the number of 6-components of $Y(p)$ intersecting with $X(p)$, or zero otherwise.

Theorem 2—The number of cavities $\delta(p)$ is one when all the 6-neighbors of p are object voxels and zero otherwise.

Rigorous proofs for these theorems may be found in Saha and Rosenfeld [63] while more intuitive and illustrative clarifications are presented in [49]. Intuitively, a voxel p is a "simple voxel" if and only if its binary transformation (i.e., conversion from object voxel to a background voxel or vice versa) does not alter digital topology of an object. Following Saha *et al.* [48, 64–65], a voxel p is a (26,6)-simple voxel if and only if the number of object component $\xi(p)$ in $\mathcal{N}^*(p)$ is exactly one and the number of tunnels $\eta(p)$ and the number of cavities $\delta(p)$ in $\mathcal{N}^*(p)$ are both zero. An efficient solution for computing both (26,6)-simple voxels and local topological parameters $\xi(p)$, $\eta(p)$ and $\delta(p)$ was presented in [48–49, 63] using the notions of dead faces, dead edges, effective voxels and geometric classes of $3 \times 3 \times 3$ neighborhood. In the following, first, we briefly review the DTA method as the developments in subsequent sections are dependent on several theoretical ideas of DTA.

2.2 Digital Topological Analysis

The primary objective of digital topological analysis or DTA is to uniquely determine the topological class of each voxel in a skeletal representation of a 3D object. The method was originally invented by Saha and Chaudhuri [48] and later adopted in the context of trabecular bone image analysis [49–50, 66]. Theory and methods behind DTA have been thoroughly described in [48–49]. For the sake of brevity, here, we only describe some basic ideas necessary to understand the developments in the following sections. Let us explain the idea on an object $\mathcal{S} \subset \mathbb{R}^3$ that may be represented as a union of finitely many surfaces and curves in a continuous 3D-space (see Figure 4(a)). It is interesting to note that a point in $\mathcal{S}$ may be classified depending on its local topological property. For example, the removal of a point p_s on a surface of $\mathcal{S}$ creates exactly one tunnel in a sufficiently small neighborhood of that point. The removal of a point p_{ss} on a junction of multiple surfaces creates multiple tunnels. It creates exactly two objects on a curve (p_c) and multiple objects at a junction of curves (p_{cc}). At a junction of surface and curve (p_{sc}), it creates multiple objects and exactly one tunnel and so on.

In a digital space, we indentify eight different topological classes of skeletal voxels, namely, isolated, curve interiors, curve edges, surface interiors, surface edges, and curve-curve, surface-curve, and surface-surface junctions (Figure 4(b)). However, the classification in a digital space is not as straightforward as in the case of $\mathbb{R}^3$. DTA is solved in three sequential steps – (1) determination of local topological type, (2) initial topological classification based on these types and (3) final classification after corrections at different topological junctions. Local topological type [48] provides only a partial classification which is essentially derived from the three local topological parameters $\xi(p)$, $\eta(p)$ and $\delta(p)$. During the second step, a unique initial classification is achieved by reviewing the local topological type of 26-neighbors of each voxel not uniquely classified during the first step. After initial classification, the process is complete except for some possible corrections at junctions. This step is primarily accomplished by analyzing the topology of edge type voxels and the fact that, under a normal circumstance, edge voxels on a surface form a 26-closed curve and this normal topology of edge voxels is perturbed only at junctions.

2.3 Manifold Distance Transform

In this section, we present the theory and algorithm for a new distance transform that may be useful to analyze and derive quantitative measures related to geodesic geometry of a digital shape. In the literature of digital topology, “geodesic distance” has been used to represent the constrained distance between two points inside a connected region in a 2D digital space [67–68]. Specifically, “geodesic distance” between two pixels inside a given region represents the length of the shortest path between the two pixels under the constraint that the path lies entirely inside the region. Piper and Granum [69] studied the properties of such paths in convex and concave domains in 2D. Verwer *et al.* [70] presented an efficient algorithm in 2D for computing constrained distance transform of a binary reference image where the paths are not allowed to enter into the background of another constraint image. Here, we define a distance between two voxels on a digital surface, say S, which is an union of finitely many digital manifolds embedded in 3D and formulate a distance transform that, essentially, computes geodesic distance (in the true sense) of a voxel $p \in S$ from the nearest edge of S. To avoid conflicts with existing terminologies, we will refer to it as “manifold distance transform” or “MDT” in short. Kimmel and Sethian [71] presented an elegant algorithm for computing shortest path length on a triangulated manifold often, generated by marching cube algorithm [72]. This method has been applied for analyzing geometry of sulcal regions on cortical surface [73–75]. However, none of the above works have discussed distance transform on a digital manifold which is essential to analyze the geometry and topology of surface like structures or structures consisting of plates and rods (e.g., a trabecular bone network) directly from their digital representation. It may be pointed out that triangulated manifold representation require binarization; on the other hand,

digital representations are capable of directly handling fuzzy representation of an object. Therefore, such digital manifold distance transform may potentially be useful to analyze geodesic geometry of fuzzy objects which may be a research topic of its own and not addressed in the current paper. In the following, we formally define manifold distance transform and present an algorithm.

A (26,6)-*digital surface* is a nonempty set S of voxels where each (26,6)-simple voxel [48, 64–65] $p \in S$ has at least one pair of opposite 6-neighbors in the background $\bar{S}$; such digital surfaces are often obtained by applying skeletonization on binary or fuzzy digital images. *Manifold distance transform* is a function $MDT{:}S \rightarrow \mathbb{R}$, where S denotes a digital surface and, $\forall\ p, \in S$, $MDT(p)$ provides the "manifold distance" between p and the edge of S (see Figure 4(b) for examples of edges on a digital surface). First, let us consider the situation where S is a digital surface containing no junction voxel (see Figure 4(b) for examples of junctions on a digital surface); such a digital surface will be referred to as a (26,6)-*digital manifold*. Let S_E denote the set of all edge voxels on S. Between any two voxels $p, q \in S$, there may be infinitely many 26-paths in S; let $\mathcal{P}(p, q, S)$ denote the set of all such paths from p to q in S. The length of a path $\pi = \langle p = p_0, p_1, \ldots, pn = q \rangle$, denoted by $\Pi(\pi)$, is defined as follow:

$$\Pi(\pi) = \sum_{i=0}^{n-1} |p_i - p_{i+1}|.$$

The manifold distance between two voxels p, q on a (26,6)-digital manifold S, denoted as $\mathcal{D}(p, q, S)$, is defined as follows:

$$\mathcal{D}(p, q, S) = \min_{\pi \in \mathcal{P}(p,q,S)} \Pi(\pi).$$

It may be shown that, for any (26,6)-digital manifold S, the manifold distance $\mathcal{D}$ satisfies the required metric property. MDT may be computed by initializing its values at edge voxels S_E and then propagating the MDT values into inner voxels along S using an wave-propagation algorithm similar to the one followed in fuzzy connectivity or fuzzy distance transform methods [76–78]. However, the skeleton of a real object generally contains junctions and we can consider a skeleton as a union of finitely many digital manifolds glued at junctions. Intuitively, a junction may be formed as a voxel (e.g., junction between multiple curves or between a curve and a surface) or a path of voxels (e.g., junction between multiple surfaces) at the intersection of multiple digital manifolds. Illustrations of different types of junctions on a digital surface are presented in Figure 4(b); see [48] for formal definitions. Skeletons of real objects consist of multiple digital manifolds attached at junctions and it is important to maintain the identity of individual manifolds during MDT computation. As illustrated in Figure 5(a), individual manifolds lose their identities when MDT values are allowed to propagate along paths crossing junctions leading to artifacts in MDT values. For example, the central portion of the base surface in the figure artificially inherits lower MDT values (reddish color) from the vertical segment. Such artifacts are rectified (Figure 5(b)) by imposing a validity condition on 26-paths as follows. Let S denote the set of all voxels in a (26,6)-digital surface representing the skeleton of some object, say O. Let $S_J \subset S$ denote the set of all junction voxels on the skeleton S; S_J may be determined using the DTA method [48] reviewed in Section 2.2. A 26-path $\pi = \langle = p_0, p_1, \ldots, p_n = q \rangle$ between two voxels $p, q \in S$ is called a *26-valid path in S* if – (1) $\forall i = 1,2, \ldots, n-1$, $p_i \in S - S_J$ and (2) $\nexists r \in S_J$ and $0 \leq i < n$ such that $|p_i - p_{i+1}| > \max(|p_i - r|, |r - p_{i+1}|)$. A violation of the second condition of a path is considered as a "crossing" with a junction without sharing a common voxel, because, the path $\ldots, p_i, r, p_{i+1}, \ldots$ is more natural as compared to the path $\ldots, p_i, p_{i+1}, \ldots$ in the sense that the former path accomplishes the move from p_i to p_{i+1}

using shorter steps. An example of such crossing between a 26-path π (the path of red voxels) and a junction line l_J (the path of blue voxels) is illustrated in Figure 5(c) where π and l_J have no common voxel. The algorithm for computing MDT for a (26,6)-digital surface is presented in the following. Here, by ordinary distance transform, we refer to either binary or fuzzy distance transform [76, 79–81] where the distance feature values are initialized at every voxel in the background of an object O. In our current implementation, fuzzy distance transform is used for initialization. An example of manifold distance transform computation is presented in Figure 2(e). Here, we have used a surface rendition technique instead of voxel rendition used for Figure 2(a–d) as color variations are better rendered in surface display as compared to the voxel mode. It may be noted that colors at surface edges are not always strongly red as MDT values at edges are initialized as the value of local thickness. This method of initialization allows us to capture the local width of a volumetric structure in VTA and not the skeletal structure as discussed at the beginning of Section 2.

```
begin
process compute_MDT
input:
a (26,6)-digital surface S
// S may be obtained by skeletonizing a binary digital object O □ □3
set of junction voxels SJ □ S
set of edge voxels SE □ S
ordinary distance transform DT: O → □
output:
manifold distance transform MDT: S → □
auxiliary data structure:
a sequential queue Q
for each voxel p □ S
assign MDT (p) = max_MDT_value
for each voxel p in SE
assign MDT(p) = DT(p)
push p in Q
while
Q is not empty
pop a voxel p from Q
for each voxel q □ 𝒩* (p)
define link (p, q) = |p – q|
if
q □ SJ AND MDT (q) < MDT (p) + link (p, q)
assign MDT (q) = MDT (p) + link (p, q)
else if
MDT (q) < MDT (p) + link (p, q)
AND □r □ SJ that |p – q| > (|p – q|, r| – q|)
assign MDT (q) = MDT (p) + link (p, q)
push q in Q
end process compute_MDT
```

It may be mentioned that, in the above algorithm, the definition of the set S_E of edge voxels may be altered as per the requirement of an application. For example, S_E may be – (1) the set of all surface- and curve-edge voxels or (2) the set of all surface- and curve-edge, curve-interior, and curve-curve junction voxels.

2.4 Skeletonization

Here, we adopt a previously reported skeletonization method [53] which completes the skeletonization process in two steps – primary and secondary skeletonization. Primary skeletonization iteratively erodes object voxels from the current outer layer of an object while preserving its topology and so-called "shape". In order to preserve object topology, only (26,6)-simple voxels [64–65] are considered for erosion. Both surface- and arc-like shape voxels [53] are preserved during the erosion process. The output of primary skeletonization may contain two-voxel thick surfaces and curves. Extra thick voxels [53] are removed using an extra iteration referred to as secondary skeletonization. The output of the method is presented in Figure 2(b). Although, the method attempts to reduce effects of noise in a skeleton, it does so only using local context of object geometry and therefore, is destined to perform sub-optimally. Here, we describe a new post-skeletonization algorithm to identify and eliminate noisy branches in a skeleton. Unlike, the noise removal approaches, generally adopted within a skeletonization algorithm, the current method identifies noise based on global context of skeletal geometry as described in the following.

Let S denote the skeleton of an object O derived using the above algorithm. The basic idea here is to distinguish skeletal branches contributed by true geometric features in the original object from those originated by noisy bumps or dents, often, common in digital images. However, often, a small branch originating from a one- or two-voxel protrusion grows iteratively due to the topology preservation constraint and eventually leads to a long branch in the final skeleton (see Figure 6). Frequently, such branches appear to be an important feature in a skeleton and may not be recognized as a noisy branch without additional information. To overcome this problem, in a skeletal branch, we distinguish voxels needed to maintain object shape features from those survived merely for topology preservation. Fortunately, the skeletonization method adopted here keeps track of voxels surviving for shape preservation. We refer to such voxels as *shape voxel*s and use S_S to denote the set of all shape voxels in a skeleton S. In order to determine the importance of a branch in a skeleton, we introduce a new "shape distance transform" which is essentially a modification of MDT. The idea of shape distance transform (*STD*) may be better understood using an example as illustrated in Figure 6. Let us consider a linear digital shape as shown in the figure that contains a noisy pixel. Following that shape pixels/voxels are always defined locally, a noisy pixel/voxel may slip through the constraint of a shape pixel/voxel. Depending upon the constraints for a shape point, it is always possible to create an example of a noisy protrusion that is wrongly chosen as a shape pixel/voxel. Here, we have used a simple example as our main intension is to illustrate the idea of SDT. Although, only one pixel in a noisy protrusion is selected as a shape pixel, it leads to a long branch in the final skeleton caused by topology preservation. Therefore, just by looking at the skeleton, it s often difficult to decide whether a branch is caused by noisy protrusion or it carries meaningful information of the original shape. We formulate SDT such that only shape pixels/voxels contribute to the "shape length" of a path (or a branch) and the pixels/voxels survived merely because of topology preservation are ignored. Thus only one pixel will contribute to shape length of the path π that later makes it easy to decide the path as a noisy branch. Shape length is formulated using a new membership function μ_{S_S} which takes '1' value when a voxel is a shape voxel and '0', otherwise.

In order to formally defined shape distance, first, we define a modified set of edge voxels S_E. from which shape distance transform is computed. Intuitively, S_E. should constitute of all surface- and curve-edge voxels identified using DTA. However, in a TB network, two-voxel wide ribbon-like structures appear and should be treated separately as follows. A surface-edge voxel with no surface-interior voxel in its $3 \times 3 \times 3$ neighborhood is reclassified as a *profile* voxel [49]. Profile voxels form a two-voxel-wide ribbon-like structure and we need to remove a pair of voxels to disconnect the structure into two except at its edges; based on this

observation, profile edges are defined as follows. Let p be a profile voxel in S; we call p as a *profile-edge* voxel if $\forall\, q \in \mathcal{N}(p) \cap (S - \{p\})$, q is a (26,6)-simple voxel in $S - \{p\}$. The set of edge voxels S_E is the set of all surface-, curve-, and profile-edge voxels; note that non-edge profile voxels are no longer surface-edge voxels and therefore, is not included in S_E. *Shape length* of any 26-valid path $\pi = \langle p_0, p1, \ldots, p_n \rangle$ on a skeleton S, denoted by $\Pi_{S_S}(\pi)$is defined as follows:

$$\Pi_{s_S}(\pi) = \sum_{i=0}^{n-1} \frac{1}{2}\left(\mu_{s_S}(p_i) + \mu_{s_S}(p_{i+1})\right)|p_i - p_{i+1}|,$$

$$\text{where } \mu_{s_S}(p) = \begin{cases} 1, & \text{if } p \in S_s, \\ 0, & \text{otherwise.} \end{cases}$$

Shape distance transform or *SDT* is a function $SDT: S \rightarrow \mathbb{R}$, where $SDT(p)$ gives the shape length of the shortest 26-valid path in S between p and the edge S_E of the digital surface S; if there is no 26-valid path from p to S_E, $SDT(p)$ is set to $+\infty$. The algorithm of computing shape distance transform is exactly the same as the process compute_MDT except that the definition of $link(p, q)$ is modified to $link(p,q) = \frac{1}{2}\left(\mu_{s_S}(p) + \mu_{s_S}(q)\right)|p - q|$ following the spirit of the above equation. Finally, noise pruning is accomplished using the following algorithm.

```
begin
process compute_noise_pruning
input:
a skeleton S
set of junction voxels S_J ⊂ S
shape distance transform SDT S → ℝ
a predefined threshold thr
output:
noise pruned skeleton S'
assign a temporary skeleton tS = S
for each voxel p ∈ S_J
for each voxel q ∈ N*(p) ∩ S – S_J
if SDT (q) < thr
assign tS = tS –{q}
assign a set of seed voxels S_d as follows
S_d = {p∈p ∈ tS and SDT (p) ≥ thr}
assign the noise pruned skeleton S' as follows
S' = {p∈p ∈ tS and p is 26-connected to S_d in tS}
augment S' as follows
S' = S' ∪ {p∈p ∈ S_J and p is 26-adjacent to S' – S_J}
end
process compute_noise_pruning
```

The key idea behind the above noise pruning algorithm is to first unglue skeletal branches at junctions and then retrieve the meaningful branches using a connectivity analysis from seeds carrying significant shape information. The last augmentation step in the algorithm is used to retrieve the part of a meaningful branch lost during the process of ungluing. The result of noise pruning is illustrated in Figure 2(b). Here, we have used *thr* = 2 voxel units.

2.5 Manifold scale

Manifold scale denotes the geodesic width of the local surface at each voxel on a digital surface and is computed in two steps – (1) initiate manifold scale at each axial voxel p as $MDT(p)$ and (2) inherit manifold scale at a non-axial voxel from its nearest axial voxel. Often, the arc-skeleton [53] derived from a digital surface S is used to represent the set of axial voxels of S. However, in the present context, arc-skeleton may not be the best choice as a noisy protrusion may extend a long branch all the way to a deeper axial line due to the topology preservation constraint [64–65] and thus affecting manifold scales of more voxels. Therefore, instead of computing an arc-skeleton, we identify only those voxels representing local elongatedness of S. Specifically, we consider axial voxels as the set of all arc-shape voxels which is a modified version of the original definition presented in [53].

The definition of arc-shape voxels is best understood in the context of a hypothetical erosion process of a digital surface S in an increasing order of MDT values. Let $p(x_1, x_2, x_3)$ be a voxel in S. At the time of finding whether or not p is an arc-shape voxel, all voxels $q \in S$ with $MDT(q)$ $MDT(p)$ have already been checked and some of those voxels may have been marked as arc-shape voxels. Also, at the time p is being checked, all unmarked voxels with their MDT values less $MDT(p)$ are hypothetically removed as background voxels. With this context in mind, let us define arc-shape voxels as follows. A voxel p may satisfy the arc-shape constraint along any of the three coordinate axis directions; let us consider the first coordinate axis. A *middle plane* orthogonal to the first coordinate axis and passing through the voxel p is denoted by $\mathcal{M}_1(p)$ and is defined as the set of all voxels with their first coordinate value equal to that of p, i.e. $\mathcal{M}_1(p) = \{(x_1, y_2, y_3) | y_2, y_3 \in \mathbb{Z}\}$. Similarly, the *upper* and *lower planes* of p orthogonal to the first coordinate axis, denoted by $\mathcal{U}_1(p)$ and $\mathcal{L}_1(p)$, respectively, are defined as $\mathcal{U}_1(p) = \{(x_1 + 1, y_2, y_3) | y_2, y_3 \in \mathbb{Z}\}$ and $\mathcal{L}_1(p) = \{(x_1 - 1, y_2, y_3) | y2, y3 \in \mathbb{Z}\}$. The 2×2 neighborhood of p on $\mathcal{M}_1(p)$ is the set of the voxels $\{(x_1, x_2, x_3), (x_1, x_2 + 1, x_3), (x_1, x_2, x_3 + 1), (x_1, x_2, +1, x_3 + 1)\}$; let $A_1(p)$ denote the set of all voxels in this 2×2 neighborhood with their MDT values no less than $MDT(p)$ or already marked as an arc-shape voxel. A voxel p is an *arc-shape* voxel along the first coordinate axis direction if it satisfies all the following three conditions.

1. $\forall q \in (\cup_{r \in A1(p)} \mathcal{N}(r) - A1(p)) \cap \mathcal{M}_1(p)$, $MDT(q) < MDT(p)$ is not marked as an arc-shape voxel.
2. $\exists q \in \mathcal{N}(p) \cap \mathcal{U}_1(p)$ such that

$$MDT(q) \geq MDT(p) \text{ or } q \text{ is already marked as an arc} - \text{shape voxel.}$$

3. $\exists q \in \mathcal{N}(p) \cap \mathcal{L}_1(p)$ such

$$MDT(q) \geq MDT(p) \text{ or } q \text{ is already marked as an arc} - \text{shape voxel.}$$

The first condition ensures that there exists a 6-closed path of current background voxel around p on the middle plane $\mathcal{M}_1(p)$. The second and third conditions ensure that at least one voxel on each of the planes $\mathcal{U}_1(p)$ and $\mathcal{L}_1(p)$, at the vicinity of p, survives while the voxel p is considered for hypothetical erosion or marking. An illustrative description of arc-shape voxels is presented in Saha *et al.* [53]. Arc-shape voxels along the directions of the second and third coordinate axes are defined similarly. (S) is used to denote the set of all axial or arc-shape voxels on a skeleton S; note that a skeleton is essentially a (26,6)-digital surface.

Manifold scale at an axial voxel $p \in Axial(S)$, denoted by $MS(p)$, is directly determined as the MDT value of p. For a non-axial voxel $q \in S - Axial(S)$, its manifold scale $MS(q)$ is inherited

from its nearest axial voxel. Manifold scale is computed using an algorithm similar to compute_MDT as follows:

```
begin
process compute_Manifold_Scale
input:
a skeleton S
set of junction voxels S_J ⊂ S
set of axial voxels (S)
manifold distance transform MDT: S → ℝ
output:
nearest axial voxel mapping NAV: S → Axial (S)
manifold scale MS: S → ℝ
auxiliary data structure:
auxiliary manifold distance measure aMDM from axial voxels
a sequential queue Q
for all voxels p ∈ S
assign aMDM (p) = max_value
for all voxels p ∈ Axial (S)
assign aMDM (p) = −MDT (p)
assign NAV (p) = p
push p in Q
while
Q is not empty
pop a voxel p from Q
for all voxels q ∈ 𝒩* (p)if
q ∈ S_J AND aMDM (q) > aMDM (p) + |p − q|
assign aMDM (q) = aMDM (p) + |p − q|
assign NAV (q) = NAV (p)
else if
aMDM (q) >aMDM (p) + |p −q|
AND ∃r ∈ S_J such that |p − q| > max(|p − r|, |q − r|)
assign aMDM (q) = aMDM (p) + |p − q|
assign NAV (q) = NAV (p)
push q in Q
for all voxels p ∈ S
assign MS(p) = MDT(NAV(p))
end process compute_Manifold_Scale
```

In the above algorithm, the step "assign *aMDM* (*p*) = −MDT " reduces the domain of noisy axial voxels as such voxels are commonly associated with smaller MDT values. Here, it s worth mentioning that the MDT map used in the above algorithm as an input is computed with the set S_E of edge voxels (see Section 2.3) as the set of all *SE*-, *C*-, *CE*-, *CC*- and profile-type voxels in the skeleton; also, for a *C*-, *CE*-, *CC*- or profile-type voxel, its MDT value is initiated as twice the local fuzzy distance transform value to capture structure width. The result of application of the method on a small region taken from a TB μCT image is illustrated in Figure 2(f).

2.6 Volumetric Feature Propagation

As described above, manifold scale essentially resembles a manifold topological characterization at each skeletal voxel. Further, this manifold topological characterization

immediately maps a voxel on the continuum between perfect plates and rods. The aim of the current step is to propagate manifold scale or topological characterization from skeleton to the entire TB volume leading to volumetric topological analysis or VTA. Bonnassie *et al.* [44] proposed a feature propagation method from skeletal voxels to entire volume by copying feature values from a skeletal voxel p to all voxels within the maximal ball centered at p. However, as mentioned by the authors, the method suffers from the fact that final results depend on the order in which skeletal voxels are processed. Here, we provide a classical solution to this problem using nearest neighbor approach that is independent of such scan or processing order.

VTA produces a function $VTA: O \rightarrow \mathbb{R}$ that assigns a topological classification at each voxel p in a digital object O on the continuum between a plate and a rod. Differently, at each TB voxel, VTA is capable to delivering the measure of the local TB width in micrometer. Similar to manifold scale, computation of VTA is accomplished using the following steps – (1) initiate $VTA(p)$ at each voxel p on the skeletal S of O as the manifold scale $MS(q)$ of p and (2) at a non-skeletal voxel q, inherit $VTA(q)$ from its nearest skeletal voxel. The algorithm for volumetric feature propagation is exactly the same as that of manifold scale computation except the following differences – (1) at each skeletal voxel p, the auxiliary distance measure $aDM(p)$ is initiated as '$-DT(p)$', (2) no extra constraint related to junction crossing is needed and (3) at each voxel $p \in V$, its VTA value is assigned as the manifold scale value of the nearest skeletal voxel. Final VTA results are presented in Figure 2(g,h) from two different view angles.

2.7 Normalized Plateness and Rodness Measures

The *VTA* algorithm described in the previous subsection may be assigned with a unit of millimeter by expressing the Euclidean distance $|p - q|$ between two voxels p, q in millimeter as per image resolution. Here, we define two normalized measures of plateness and rodness on the basis of the image-derived *VTA* function as follows:

$$plateness(p) = \begin{cases} 0, & \text{if } VTA(p) < \text{plate}_{\min}, \\ 1, & \text{if } VTA(p) > \text{plate}_{\max}, \\ \frac{VTA(p) - \text{plate}_{\min}}{\text{plate}_{\max} - \text{plate}_{\min}}, & \text{otherwise}, \end{cases}$$

$$rodness(p) = 1 - plateness(p).$$

and,

Here, we have used $\text{plate}_{\min} = 0.15$ mm and $\text{plate}_{\max} = 1$ mm. The minimum value of TB plate width is determined by voxel size (here, 0.15 mm) and the upper bound was determined by finding TB width at upper 97 percentile for the specimens used in our experiments. It may be noted that no abrupt change in plateness/rodness values takes place at lower or upper ends; rather it causes saturations at two ends, namely, $\text{plate}_{\min}$ and $\text{plate}_{\max}$. Selection of the upper bound at 97 percentile essentially ignores variations of plate width within upper three percentile data putting saturation at 97 percentile. Therefore, the loss of data due to the normalization step is minimal. It is worth mentioning that the normalization process described here may not be optimum. Optimization of the normalization scale and, more importantly, the relation of normalized plateness/rodness measures with different disease status need to be carefully evaluated in a large patient study which is beyond the scope of the current paper.

3 EXPERIMENTAL PLANS AND METHODS

In this section, we describe our experimental plans and methods to examine the performance of the VTA method and to compare it with bone volume/total volume (BV/TV), a representative image-based measure for BMD, and DTA measures. Specifically, we examine the accuracy of

the VTA method on computational phantom images of sinusoidal cross-plates of varying width and quantitatively evaluate both intra- and inter-modality reproducibility of the method using multi-scan CT and μCT imaging. Also, we examine the method s ability to predict experimental biomechanical properties of TB via CT imaging under *in vivo* conditions. In the following, we describe the detail plans and methods for all three experiments.

3.1 Accuracy Analysis on Phantom Images

Accuracy of the method has been examined quantitatively on computational phantoms (Figure 7). Twenty phantom images, each containing sinusoidal cross plates of known plate width, were computer-generated. Initially, the phantom images were generated at a high isotropic resolution of 50 μm and TB thickness of 200 μm. These high resolution images were down-sampled at 150 μm isotropic voxel size to simulate partial volume effects. Each down-sampled image was further degraded with additive random noise at SNR of 12. One cross sectional image of a phantom is illustrated in Figure 7(a). A bone volume fraction image (Figure 7(b)) was computed from each of these phantom images and was subsequently binarized using thresholding. Mean plate width was computed for each binarized image using VTA and the linear correlation between the known plate width and computed plate width was examined.

3.2 Intra and Inter-Modality Reproducibility

Both intra- and inter-modality reproducibility of VTA have been quantitatively examined and compared with those of BV/TV and DTA measures using repeat CT scans and μCT imaging of four cadaveric distal tibia specimens. In the following, we describe the CT and μCT imaging protocols and the data analysis procedures adopted for these experiments.

3.2.1 CT and μCT Imaging—Four cadaveric distal tibia specimens were scanned in a Siemens Sensation 64 Multi-slice CT scanner at 120 kVp, 140 mAs, and pitch of 0.8 to adequately visualize bony structures. After scanning each specimen in a helical mode with a slice thickness of 0.6 mm and collimation of 12 × 0.6 min, data was reconstructed at 0.3 mm slice thickness using a normal cone beam method with a special U75 kernel to achieve high structural resolution. In the rest of this paper, by “CT”, we will understand “multi-slice CT” unless stated otherwise. Three repeat CT scans of each distal tibia specimen were acquired after repositioning the specimen on the CT table before each scan. Image parameters for these scans were as follow: matrix size = 512 × 512 pixels; slice-thickness = 0.3 mm; pixel size = 0.15 mm. Each distal tibia specimen was also scanned on an Imtek Micro-cat II producing images at 28.8 μm isotropic resolution after removing soft tissue and dislocating tibia from the ankle joint. Three repeat CT scans of each of the four specimens were used to examine intra-modality reproducibility while the first CT scan and the μCT data of all specimens were used for evaluating inter-modality reproducibility.

3.2.2 Image Processing and Data Analysis—A total of twenty five cylindrical VOIs, each of 3.75 mm radius and length, were randomly located in the first CT scan of four distal tibia specimens. For each cylinder, its axis was aligned along the scan direction and the base was randomly located above the position 8 mm proximal to the distal cortical endplate visually identified in the image. Each of the other two repeat CT and the single μCT images of each specimen were registered with the first CT image of the same specimen using the registration graphical tools supported by the Analyze software. Each image data set was processed through the following cascade of steps – (1) computation of bone volume fraction (BVF) image from each of CT/μCT images using a step-up ramp function, (2) resampling of BVF images at 0.15 mm isotropic voxel using the windowed sinc interpolation method [82], (3) registration of the BVF image derived from each of the second and third repeat CT and the μCT scans with that from the first CT scan, and (4) application of DTA and VTA methods to each of the resampled

and registered BVF images. Following the fact that TB region consists of marrow and bone only, a step-up ramp is a natural choice to determine partial occupancy of bone in a voxel via CT imaging [83]. In the literature, binary thresholding has been adopted to segment trabecular bone region in CT and μCT imaging [1, 25–26]. Here, we have adopted a soft thresholding using a step-up ramp function for BVF computation [24, 58] to capture partial volume effects.

In each VOI, the following TB measures were computed from all repeat CT and μCT images – (1) bone volume/tissue volume or BV/TV, (2) surface to curve ratio SCR_{DTA} and (3) erosion index EI_{DTA} using DTA, and (4) average surface-width SW_{VTA} and (5) surface to curve ratio SCR_{VTA} using VTA. Two DTA-based measures were computed according to the descriptions presented in [49, 66]. Here, we briefly describe the computation process for three other TB measures. Let *V* denote the set of voxels representing a VOI over which TB measures are computed and let *BVF*(*p*) denote the normalized BVF value at a voxel *p*, i.e., $0 \leq BVF(p) \leq 1$. Computations of *VTA*, *plateness*, and *rodness* measures were discussed in Section 2. In the following, we define three TB measures, namely, BV/TV, SW_{VTA}, and SCR_{VTA}, that are computed over the VOI *V*. It may be noted that the surface width measure SW_{VTA} is expressed in the unit of microns and is independent of soft thresholding technique used for *plateness*, and *rodness* measures.

$$\mathrm{BV/TV} = \frac{\sum_{p \in V} BVF(p)}{\|V\|},$$
$$\mathrm{SW_{VTA}} = \frac{\sum_{p \in V} VTA(p) BVF(p)}{\sum_{p \in V} BVF(p)},$$
$$\mathrm{SCR_{VTA}} = \frac{\sum_{p \in V} plateness(p) BVF(p)}{\sum_{p \in V} rodness(p) BVF(p)}.$$

3.3 Predictability of Experimental Biomechanical Properties of TB

The purpose of this experiment was to evaluate the ability of each imaging measure to predict biomechanical properties of TB specimens as determined experimentally using compressive mechanical testing. Eight fresh-frozen cadaveric forearms were collected from the University of Iowa s Deeded Bodies Program. No age or sex information was available for these specimens. Among the eight TB specimens prepared as described below, three were rejected as being too porotic for testing, so experimental data from five specimens are presented here. CT imaging was first performed on these specimens using the same protocol described in Section 3.2.1. The forearm specimens were then frozen until the test specimens were prepared.

3.3.1 Biomechanical experiments—A cylindrical core was harvested from each distal radius specimen, and two compressive mechanical tests were performed on each core. Due to the limited length of TB cores achievable at the distal radius, compression testing with platens [84] was used instead of an endcap technique [85]. The first test was performed to determine Young's modulus (E) by measuring strain with an extensometer on the specimen (Figure 8a), while the second test was performed to determine yield stress by measuring strain with the testing machine at the compressing platens (Figure 8b). The second test was performed because during the first test, most of the TB cores failed at a specimen end rather than within the extensometer span; specimen lengths were therefore shortened to obtain more homogeneous properties across each length. All specimen preparation and mechanical testing were performed at the University of Iowa s Orthopaedic Biomechanics Laboratory.

3.3.1.1 Specimen preparation: Cylindrical TB specimens of nominally 8 mm in diameter were cored from distal radii *in situ* along the proximal-distal direction. A-P and M-L radiographs were first used to determine the plane of an initial distal cut done to eliminate the

growth plate from a test specimen, and then to determine the central axis of the bone and thus the core location. Each specimen was cored with saline immersion using an 8.25 mm inner diameter diamond coring bit (Starlite Industries, Rosemont, PA). The core was released from the distal radius by cutting it with a razor saw, and the specimen ends were sanded smooth, flat, and parallel. Specimen length and diameter were measured three times and averaged, and the middle 6 mm of the specimen length was marked for extensometer attachment position. Each core was wrapped in saline-soaked gauze, and frozen until thawed for testing. For the non-extensometer testing, the specimen ends were again sanded to remove damaged bone from the specimen ends. For extensometer testing, a minimum specimen length of 18 mm was desired, to achieve both the minimum aspect ratio of 2:1 recommended for TB compression specimens [84] and a 3:1 ratio of specimen length to extensometer gage length used in an earlier study [84]. (One specimen did not achieve this minimum specimen length; because of poor bone quality resulting in bone damage during specimen preparation, its length was 15.9 mm.) For the subsequent non-extensometer testing, specimen length was dependent on how much bone needed to be removed from the damaged ends; the resulting aspect ratios were all greater than 1:1.

3.3.1.2 Mechanical testing of TB specimens: The TB cores were mechanically tested in compression using an electromechanical materials testing machine (MTS Insight, MTS Systems Corp., Eden Prairie, MN). Each specimen was placed between unlubricated, polished, plano-parallel steel platens. For the first test, to minimize specimen end effects, strain was measured with a 6 mm gage length extensometer (model 632.29F-30, MTS Systems Corp., Eden Prairie, MN) attached directly to the midsection of the bone (Figure 8a). For the second test, strain was measured with the testing machine at the compressing platens (Figure 8b). A compressive preload of 10 N was applied and strains then set to zero. At a strain rate of 0.005 sec^{-1}, each specimen was preconditioned to a low strain with at least ten cycles and then loaded to failure. Young's modulus (E) was determined for each specimen as the highest 20% section slope of the stress-strain curve. Yield stress was determined as the intersection of the stress-strain curve and a 0.2% strain offset of the modulus.

3.3.2 Image Processing and Data Analysis—Each CT image data set was processed through the same cascade of image processing steps described in Section 3.2.2. For each specimen, two VOIs were manually determined using the graphical interface supported by the Analyze software. Size and location of these VOIs were chosen as par the information recoded during specimen preparation for each experiment. The first VOI was used for computing TB measures to examine their abilities to predict Young's modulus while the other VOI was used for comparison with yield stress. For both VOIs, a cylinder of 8 mm diameter was used and was first visually aligned along the forearm axis. Subsequently, the proximal end of the cylinder was positioned at the center of cortical rim at corresponding slice location using in-plane translations. Finally, the location of the distal end of the VOI cylinder in the slice direction and its length were determined as par the recorded core location and length. For comparison with Young's modulus, the VOI was selected as the central 6 mm region from a cylinder (length as per the recorded specimen length for the extensometer test) with its distal end located at 2mm proximal of growth plate identified visually. Growth plate was visually located on a CT image of each specimen. For comparison with yield stress, the VOI was selected as a cylinder (length as per the recorded specimen length for the platen test) located at 4 mm proximal to the growth plate. Finally, five different TB measures, mentioned in Section 3.2.2, were computed over each selected VOI and used to examine their abilities to predict corresponding mechanical measures.

4 RESULTS AND DISCUSSION

Results of VTA-based classification of plates and rods for two cylinders TB specimens are illustrated in Figure 9. A common color coding scheme (Figure 9(e): green=1.0, i.e., plates; red=0.0, i.e., rods; and yellow=0.5) is used to represent the VTA based classification of trabeculae for both specimens. The specimen of Figure 9(a) represents a highly rod-like trabecular structure while that of Figure 9(b) contains a large amount of plate-like trabeculae. The color coded VTA based classifications at different TB locations in both specimens, illustrated in Figure 9(c,d), agrees with visual perception. The BV/TV for these two specimens are 0.20 and 0.33 while the average TB width, computed by VTA, are 272 μm and 492 μm, respectively.

Results of accuracy analysis on computational phantom images of sinusoidal cross plates of varying widths, described in Section 3.1, are qualitatively presented in Figure 7. An image slice from an original phantom is displayed in Figure 7(a) while the computed BVF map is shown Figure 7(b). Figure 7(d-i) present color-coded illustrations of VTA-based classification at each voxel in six different phantoms; for these images, true plate thickness was 2, 5, 9, 13, 17, and 21 voxels, respectively. Gradual changes in color are visually noticeable from Figure 7(d) to Figure 7(i). To quantitatively examine the accuracy of the method, we performed a linear correlation analysis between true structure width and computed width using VTA method was performed and the results are presented in Figure 10. As indicated in the figure, computed mean structure width showed a high correlation ($R^2 = 0.998$) with its true width.

As described in Section 3.2.2, measurements over randomly selected twenty five VOIs from post-registered repeat-scan CT and μCT images of four distal tibia specimens were used for both intra- and inter-modality reproducibility analyses. An axial and a coronal slice from the first CT scan of one distal tibia specimen are illustrated in Figure 11(a,b). TB structures are visually distinguishable in both images; also, the coronal slice shows remarkable continuity of TB structures along the slice direction. Matching axial slice from computer-registered BVF data from three repeat CT scans and the single μCT scan are presented in Figure 11(c–f). Agreement of TB structures in three repeat CT scans and the μCT scan is visually noticeable in these figures. Also, it may be noticed in these figures that the trabecular structures in CT scans are more blurred as compared to the μCT data. It is caused by relatively wide point-spread function of CT imaging which sometimes leads to false filling of narrow holes in CT imaging of TB networks (Figure 12).

A visual comparison of VTA-based TB structural classification from three repeat CT scans and μCT imaging is illustrated in Figure 12. Among the three repeat CT scans, reproducibility of both TB structures as well as their VTA-based classification of plates and rods is visually remarkable. In comparison with the μCT data, some narrow holes are filled in CT images due to the blurring caused by relatively wider point-spread function of latter imaging technology and it leads to reduced rodness in CT data. However, the overall agreement in VTA-based classification of TB structures via CT and μCT imaging is visually satisfactory. In order to quantitatively assess the intra-modality reproducibility of the methods, for each of the five TB measures mentioned in Section 3.2.2, its intra-class correlation was computed from three repeat CT scan measurements over twenty five VOIs randomly selected from four cadaveric distal tibia specimens. Graphical illustrations of repeat scan measures for five TB measures are presented in Figure 13(a–e). All the five TB measures have shown high repeat scan reproducibility in CT, although, the DTA based measures have produced slightly lower ICC values. The two VTA-based measures SW_{VTA} and SCR_{VTA} have resulted ICC values similar to that of the BV/TV measure which is expected to be a highly reproducible measure in CT imaging modality. Correlations of different TB measures in CT and μCT imaging are graphically illustrated in Figure 14(a–c). Both VTA-based measures SW_{VTA} and SCR_{VTA}

have demonstrated high correlation between CT- and μCT-derived measures and have resulted better R^2 values as compared to BV/TV and the two DTA-based measures. It may be noted in Figure 14(b) that, despite the high linear correlation between the surface width measure SW_{VTA} derived from MDCT and μCT, there is a difference in values by a factor of ~1.5 in two modalities and the same pattern is seen in Figure 14(c) with SCR_{DTA}. These results are expected since the voxel sizes are bigger in MDCT than in μCT and similar observations were found in [50].

As described in Section 3.3.1.2, two different experimental mechanical indices, namely, Youngs's modulus and yield stress, were used to evaluate the strength of each CT-derived measure to predict TB s mechanical properties. For a given CT-derived TB measure, its mean value over the corresponding VOI (see Section 3.3.2) was computed and its linear correlation with each of the two target mechanical measures was examined. Correlation of each of the three TB measures, namely, BV/TV, SW_{VTA}, and SCR_{DTA} with Young's modulus, is presented in Figure 15(a–c). The linear correlation of each of the five CT derived TB measures with Young's modulus is listed in Table 1(a). Results of correlation analysis of TB measures with yield stress are given in Figure 15(d–f) and Table 1(b). All CT-derived TB measures had good linear correlation with experimental mechanical properties of TB specimens (R^2 range: 0.782 to 0.964) except for SCR_{DTA} versus Young's modulus ($R^2 = 0.457$); see Table 1 and Figure 15. The results obtained from the limited number of specimens shows that the new method performs significantly better as compared to BMD measure BV/TV and the improvement of the new method over DTA is obvious.

Another important feature with the VTA technology is that it provides an entirely new class of information that is not deliverable using current methods. As illustrated in Figure 16, the new method is capable of delivering bone-mass distribution across various plate widths. It is notable that the bone mass to plate width distribution patterns for bones with different strengths are different. More interestingly, the bone mass distributions at low plate-width, primarily resembling rod-like trabeculae, are similar for all five TB specimens despite significantly different strengths. A possible justification behind this observation may be that, in the dynamic process of bone loss, disruptions of rods are mostly balanced with rod creations by perforations as well as erosions of plates. It will be interesting to determine a mean bone mass distribution across various plate widths for a healthy population and studying the nature of alteration of such a distribution in the process of disease progression or treatments. However, such studies are well beyond the scope of the current paper.

5 CONCLUDING REMARKS

In this paper, we have presented a new volumetric topological analysis method VTA that uniquely classifies TB topology on the continuum between perfect plates and rods at every TB location. Major novel contributions of this paper are stated in the following: (1) overall design of the method that provides a unique local classification trabecula on the continuum between perfect plates and rods via images at low resolution regime currently available through *in vivo* imaging technologies, (2) manifold distance transform for digital surfaces, (3) manifold scale, (4) a classical solution to propagate features from one set of voxels to a larger set of voxels using shortest distance approach, and (5) shape distance transform and skeletal noise pruning. Although the current method works only on binary images, the theory and algorithms directly extends to fuzzy images. Several new concepts including manifold distance transform, manifold scale and feature propagation have been introduced here along with the new development of VTA. Both intra- and inter-modality reproducibility of the method have been examined using CT repeat scans and μCT imaging of a cadaveric distal tibia specimen. Preliminary results demonstrate high intra- and inter modality reproducibility of VTA measures. The method s ability to predict TB s mechanical properties have been studied on a

limited number of cadaveric distal radius specimens and the results are promising. Results obtained from a limited number of specimens have demonstrated that the new method performs significantly better as compared to BV/TV and its improvement over DTA is obvious. Finally, VTA is suited for quantitative TB structural analysis in longitudinal as well as cross-sectional patient as well as animal studies via *in vivo* imaging.

Acknowledgments

This work was supported by NIH grant RO1 AR-054439 and internal funds from the Departments of Radiology and ECE at the University of Iowa, Iowa City, IA, USA.

References

1. Ding M, Hvid I. Quantification of age-related changes in the structure model type and trabecular thickness of human tibial cancellous bone. Bone. 2000; 26:291–5. [PubMed: 10710004]
2. Wolff, J. Das Gesetz der Transformation der Knochen. Berlin: A. Hirschwald; 1892.
3. Melton LJ 3rd. Epidemiology of spinal osteoporosis. Spine. 1997; 22:2S–11S. [PubMed: 9431638]
4. National Osteoporosis Foundation. Available: http://www.nof.org/osteoporosis/diseasefacts.htm
5. Melton LJ, Chrischilles EA, Cooper C, Lane AW, Riggs BL. Perspective. How many women have osteoporosis? Journal of Bone and Mineral Research. 1992; 7:1005–1010. [PubMed: 1414493]
6. WHO Report. Assessment of fracture risk and its application to screening for postmenopausal osteoporosis. World Health Organization; Geneva: 1994.
7. Wehrli FW, Saha PK, Gomberg BR, Song HK, Snyder PJ, Benito M, Wright A, Weening R. Role of magnetic resonance for assessing structure and function of trabecular bone. Topics in Magnetic Resonance Imaging. 2002; 13:335–356. [PubMed: 12464746]
8. Kleerekoper M, Villanueva AR, Stanciu J, Rao DS, Parfitt AM. The role of three-dimensional trabecular microstructure in the pathogenesis of vertebral compression fractures. Calcified Tissue International. 1985; 37:594–597. [PubMed: 3937580]
9. Moore R, Durbridge T, McNeil P, Parkinson I, Need A. Trabecular spacing in post-menopausal Australian women with and without vertebral fractures. Australian and New Zealand Journal of Medicine. 1992; 22:269–273. [PubMed: 1386728]
10. Recker RR. Architecture and vertebral fracture. Calcified Tissue International. 1993; 53(Suppl 1):S139–142. [PubMed: 8275368]
11. Vesterby A, Mosekilde L, Gundersen HJG, Melsen F, Mosekilde L, Holme K, Sorensen S. Biologically meaningful determinants of the in vitro strength of lumbar vertebrae. Bone. 1991; 12:219–224. [PubMed: 1910963]
12. Legrand E, Chappard D, Pascaretti C, Duquenne M, Krebs S, Rohmer V, Basle MF, Audran M. Trabecular bone microarchitecture, bone mineral density and vertebral fractures in male osteoporosis. Journal of Bone and Mineral Research. 2000; 15:13–19. [PubMed: 10646109]
13. Mosekilde L. Consequences of the remodelling process for vertebral trabecular bone structure: a scanning electron microscopy study (uncoupling of unloaded structures). Bone and Mineral. 1990; 10:13–35. [PubMed: 2397325]
14. Boutry N, Cortet B, Dubois P, Marchandise X, Cotten A. Trabecular bone structure of the calcaneus: preliminary in vivo MR imaging assessment in men with osteoporosis. Radiology. 2003; 227:708–17. [PubMed: 12676974]
15. Benito M, Gomberg B, Wehrli FW, Weening RH, Zemel B, Wright AC, Song HK, Cucchiara A, Snyder PJ. Deterioration of trabecular architecture in hypogonadal men. J Clin Endocrinol Metab. 2003; 88:1497–502. [PubMed: 12679429]
16. Chesnut CH 3rd, Majumdar S, Newitt DC, Shields A, Van Pelt J, Laschansky E, Azria M, Kriegman A, Olson M, Eriksen EF, Mindeholm L. Effects of salmon calcitonin on trabecular microarchitecture as determined by magnetic resonance imaging: results from the QUEST study. J Bone Miner Res. 2005; 20:1548–1561. [PubMed: 16059627]
17. Chavassieux, P.; Arlot, M.; Meunier, PJ. Clinical use of bone biopsy. In: Marcus, R., et al., editors. Osteoporosis. Vol. 2. New York: Academic Press; 2001. p. 501-509.

18. Recker, RR. Bone histomorphometry: techniques and interpretation. Boca Raton: CRC Press; 1983.
19. Hildebrand T, Laib A, Muller R, Dequeker J, Rüegsegger P. Direct three-dimensional morphometric analysis of human cancellous bone: microstructural data from spine, femur, iliac crest, and calcaneus. Journal of Bone Mineral Research. 1999; 14:1167–1174.
20. Boutroy S, Bouxsein ML, Munoz F, Delmas PD. In Vivo Assessment of Trabecular Bone Microarchitecture by High-Resolution Peripheral Quantitative Computed Tomography. J Clin Endocrinol Metab. 2005
21. Khosla S, Riggs BL, Atkinson EJ, Oberg AL, McDaniel LJ, Holets M, Peterson JM, Melton LJ 3rd. Effects of sex and age on bone microstructure at the ultradistal radius: a population-based noninvasive in vivo assessment. J Bone Miner Res. 2006; 21:124–31. [PubMed: 16355281]
22. Ito M, Ikeda K, Nishiguchi M, Shindo H, Uetani M, Hosoi T, Orimo H. Multi-Detector Row CT Imaging of Vertebral Microstructure for Evaluation of Fracture Risk. J Bone Miner Res. 2005; 20:1828–36. [PubMed: 16160740]
23. Graeff C, Timm W, Nickelsen TN, Farrerons J, Marin F, Barker C, Gluer CC. Monitoring teriparatide-associated changes in vertebral microstructure by high-resolution CT in vivo: results from the EUROFORS study. J Bone Miner Res. 2007; 22:1426–33. [PubMed: 17547537]
24. Saha, PK.; Saba, OI.; Hudson, M.; Pick, A.; El-Khoury, G.; Hoffman, EA. Trabecular bone structural analysis using 64 multi-detector CT scanner. 29th Annual Meeting of the American Society for Bone and Mineral Research; Honolulu, HI. 2007. p. S193
25. Bredella MA, Misra M, Miller KK, Madisch I, Sarwar A, Cheung A, Klibanski A, Gupta R. Distal radius in adolescent girls with anorexia nervosa: trabecular structure analysis with high-resolution flat-panel volume CT. Radiology. 2008; 249:938–46. [PubMed: 19011190]
26. Diederichs G, Link TM, Kentenich M, Schwieger K, Huber MB, Burghardt AJ, Majumdar S, Rogalla P, Issever AS. Assessment of trabecular bone structure of the calcaneus using multi-detector CT: correlation with microCT and biomechanical testing. Bone. 2009; 44:976–83. [PubMed: 19442610]
27. Wehrli, FW. Trabecular bone imaging. In: Young, IR., editor. Magnetic resonance imaging and spectroscopy in medicine and biology. Vol. 2. London: Wiley; 2000. p. 1356-1368.
28. Majumdar S. Magnetic resonance imaging of trabecular bone structure. Topics in Magnetic Resonance Imaging. 2002; 13:323–334. [PubMed: 12464745]
29. Wehrli FW, Saha PK, Gomberg BR, Song HK. Noninvasive assessment of bone architecture by magnetic resonance micro-imaging-based virtual bone biopsy. Proceedings of IEEE, Emerging Medical Imaging Technology, (invited paper). 2003; 91:1520–1542.
30. Link TM, Majumdar S. Osteoporosis imaging. Radiol Clin North Am. 2003; 41:813–39. [PubMed: 12899494]
31. Genant HK, Gordon C, Jiang Y, Lang TF, Link TM, Majumdar S. Advanced imaging of bone macro and micro structure. Bone. 1999; 25:149–152. [PubMed: 10423042]
32. Link TM, Vieth V, Stehling C, Lotter A, Beer A, Newitt D, Majumdar S. High-resolution MRI vs multislice spiral CT: Which technique depicts the trabecular bone structure best? Eur Radiol. 2003; 13:663–671. [PubMed: 12664101]
33. Parfitt AM, Mathews CHE, Villanueva AR, Kleerekoper M, Frame B, Rao DS. Relationships between surface, volume, and thickness of iliac trabecular bone in aging and in osteoporosis. Implications for the microanatomic and cellular mechanisms of bone loss. Journal of Clinical Investigation. 1983; 72:1396–1409. [PubMed: 6630513]
34. Vesterby A, Gundersen HJ, Melsen F. Star volume of marrow space and trabeculae of the first lumbar vertebra: sampling efficiency and biological variation. Bone. 1989; 10:7–13. [PubMed: 2660885]
35. Hahn M, Vogel M, Pompesius-Kempa M, Delling G. Trabecular bone pattern factor--a new parameter for simple quantification of bone microarchitecture. Bone. 1992; 13:327–30. [PubMed: 1389573]
36. Hildebrand T, Rüegsegger P. Quantification of bone microarchitecture with the structure model index. Computer Methods in Biomechanics and Biomedical Engineering. 1997; 1:15–23. [PubMed: 11264794]
37. Majumdar S, Newitt D, Mathur A, Osman D, Gies A, Chiu E, Lotz J, Kinney J, Genant H. Magnetic resonance imaging of trabecular bone structure in the distal radius: relationship with X-ray tomographic microscopy and biomechanics. Osteoporos Int. 1996; 6:376–85. [PubMed: 8931032]

38. Stampa B, Kuhn B, Liess C, Heller M, Gluer CC. Characterization of the integrity of three-dimensional trabecular bone microstructure by connectivity and shape analysis using high-resolution magnetic resonance imaging in vivo. Top Magn Reson Imaging. 2002; 13:357–63. [PubMed: 12464747]
39. Garrahan NJ, Mellish RW, Compston JE. A new method for the two-dimensional analysis of bone structure in human iliac crest biopsies. J Microsc. 1986; 142:341–9. [PubMed: 3735417]
40. Mellish RW, Ferguson-Pell MW, Cochran GV, Lindsay R, Dempster DW. A new manual method for assessing two-dimensional cancellous bone structure: comparison between iliac crest and lumbar vertebra. Journal of Bone and Mineral Research. 1991; 6:689–696. [PubMed: 1950674]
41. Feldkamp LA, Goldstein SA, Parfitt AM, Jesion G, Kleerekoper M. The direct examination of three-dimensional bone architecture in vitro by computed tomography. Journal of Bone and Mineral Research. 1989; 4:3–11. [PubMed: 2718776]
42. Saha, PK.; Wehrli, FW. In vivo assessment of trabecular bone architecture via three-dimensional tensor scale. SPIE: Medical Imaging; San Diego, CA. 2004. p. 750-760.
43. Vasilic B, Rajapakse CS, Wehrli FW. Classification of trabeculae into three-dimensional rodlike and platelike structures via local inertial anisotropy. Med Phys. 2009; 36:3280–91. [PubMed: 19673224]
44. Bonnassie A, Peyrin F, Attali D. A new method for analyzing local shape in three-dimensional images based on medial axis transformation. IEEE Trans Syst Man Cybern B Cybern. 2003; 33:700–5. [PubMed: 18238219]
45. Carballido-Gamio J, Krug R, Huber MB, Hyun B, Eckstein F, Majumdar S, Link TM. Geodesic topological analysis of trabecular bone microarchitecture from high-spatial resolution magnetic resonance images. Magn Reson Med. 2009; 61:448–56. [PubMed: 19161163]
46. Saha PK, Wehrli FW. A robust method for measuring trabecular bone orientation anisotropy at in vivo resolution using tensor scale. Pattern Recognition. 2004; 37:1935–1944.
47. Saha PK. Tensor scale: a local morphometric parameter with applications to computer vision and image processing. Computer Vision and Image Understanding. 2005; 99:384–413.
48. Saha PK, Chaudhuri BB. 3D digital topology under binary transformation with applications. Computer Vision and Image Understanding. 1996; 63:418–429.
49. Saha PK, Gomberg BR, Wehrli FW. Three-dimensional digital topological characterization of cancellous bone architecture. International Journal of Imaging Systems and Technology. 2000; 11:81–90.
50. Wehrli FW, Gomberg BR, Saha PK, Song HK, Hwang SN, Snyder PJ. Digital topological analysis of in vivo magnetic resonance microimages of trabecular bone reveals structural implications of osteoporosis. Journal of Bone Mineral Research. 2001; 16:1520–31.
51. Taylor, G.; Kleeman, L. Visual Perception and Robotic Manipulation : 3D Object Recognition, Tracking and Hand-Eye Coordination. Berlin: Springer; 2006.
52. Ma CM, Sonka M. A fully parallel 3D thinning algorithm and Its applications. Computer Vision Image Understanding. 1996; 64:420–433.
53. Saha PK, Chaudhuri BB, Majumder DD. A new shape preserving parallel thinning algorithm for 3D digital images. Pattern Recognition. 1997; 30:1939–1955.
54. Pudney C. Distance-ordered homotopic thinning: a skeletonization algorithm for 3D digital images. Computer Vision and Image Understanding. 1998; 72:404–413.
55. Palágyi K, Kuba A. A parallel 3D 12-subiteration thinning algorithm. Graphical Models and Image Processing. 1999; 61:199–221.
56. Chuang J-H, Tsai C-H, Ko M-C. Skeletonization of three-dimensional object using generalized potential field. IEEE Transactions On Pattern Analysis And Machine Intelligence. 2000; 22:1241–1251.
57. Hildebrand T, Rüegsegger P. A new method for the model independent assessment of thickness in three-dimensional images. Journal of Microscopy. 1997; 185:67–75.
58. Saha PK, Wehrli FW. Measurement of trabecular bone thickness in the limited resolution regime of in vivo MRI by fuzzy distance transform. IEEE Transactions on Medical Imaging. 2004; 23:53–62. [PubMed: 14719687]
59. Otsu N. A threshold selection methods from grey-level histograms. IEEE Transactions on Pattern Analysis and Machine Intelligence. 1979; 9:62–66.

60. Saha PK, Udupa JK. Optimum threshold selection using class uncertainty and region homogeneity. IEEE Transactions on Pattern Analysis and Machine Intelligence. 2001; 23:689–706.
61. Rosenfeld A. Adjacency in digital pictures. Information and Control. 1974; 26:24–33.
62. Kong TY, Rosenfeld A. Digital topology: introduction and survey. Computer Vision, Graphics, and Image Processing. 1989; 48:357–393.
63. Saha PK, Rosenfeld A. Determining simplicity and computing topological change in strongly normal partial tilings of R^2 or R^3. Pattern Recognition. 2000; 33:105–118.
64. Saha PK, Chaudhuri BB. Detection of 3D simple points for topology preserving transformation with application to thinning. IEEE Transactions on Pattern Analysis and Machine Intelligence. 1994; 16:1028–1032.
65. Saha PK, Chaudhuri BB, Chanda B, Majumder DD. Topology preservation in 3D digital space. Pattern Recognition. 1994; 27:295–300.
66. Gomberg BG, Saha PK, Song HK, Hwang SN, Wehrli FW. Topological analysis of trabecular bone MR images. IEEE Transactions on Medical Imaging. 2000; 19:166–174. [PubMed: 10875701]
67. Cárdenes R, Alberola-López C, Ruiz-Alzola J. Fast and accurate geodesic distance transform by ordered propagation. Image and Vision Computing. 2010; 28:307–316.
68. Lantuejoul C, Maisonneuve F. Geodesic methods in quantitative image analysis. Pattern Recognition. 1984; 17:177–187.
69. Piper J, Granum E. Computing distance transformations in convex and non-convex domains. Pattern Recognition. 1987; 20:599–615.
70. Verwer B, Verbeek P, Dekker S. An efficient uniform cost algorithm applied to distance transforms. IEEE Transactions on Pattern Analysis and Machine Intelligence. 1989; 11:425–429.
71. Kimmel R, Sethian JA. Computing geodesic paths on manifolds. Proc Natl Acad Sci U S A. 1998; 95:8431–5. [PubMed: 9671694]
72. Lorensen W, Cline H. Marching Cubes: a high resolution 3D surface construction Algorithm. Computer Graphics. 1987; 21:163–169.
73. Han X, Pham DL, Tosun D, Rettmann ME, Xu C, Prince JL. CRUISE: cortical reconstruction using implicit surface evolution. Neuroimage. 2004; 23:997–1012. [PubMed: 15528100]
74. Rettmann ME, Han X, Xu C, Prince JL. Automated sulcal segmentation using watersheds on the cortical surface. Neuroimage. 2002; 15:329–44. [PubMed: 11798269]
75. Tosun D, Rettmann ME, Han X, Tao X, Xu C, Resnick SM, Pham DL, Prince JL. Cortical surface segmentation and mapping. Neuroimage. 2004; 23(Suppl 1):S108–18. [PubMed: 15501080]
76. Saha PK, Wehrli FW, Gomberg BR. Fuzzy distance transform: theory, algorithms, and applications. Computer Vision and Image Understanding. 2002; 86:171–190.
77. Udupa JK, Samarasekera S. Fuzzy connectedness and object definition: theory, algorithms, and applications in image segmentation. CVGIP: Graphical Model and Image Processing. 1996; 58:246–261.
78. Udupa JK, Saha PK. Fuzzy connectedness in image segmentation. Proceedings of IEEE, Emerging Medical Imaging Technology, (invited paper). 2003; 91:1649–1669.
79. Borgefors G. Distance transformations in digital images. Computer Vision Graphics and Image Processing. 1986; 34:344–371.
80. Borgefors G. On digital distance transformation in three dimensions. Computer Vision Graphics Image Processing. 1996; 64:368–376.
81. Grevera GJ. The dead reckoning signed distance transform. Computer Vision Image Understanding. 2004; 95:317–333.
82. Thevenaz P, Blu T, Unser M. Interpolation revisited. IEEE Trans Med Imaging. 2000; 19:739–58. [PubMed: 11055789]
83. Bushberg JT, Seibert JA, EML, Boone JM. The Essential Physics of Medical Imaging.
84. Keaveny TM, Borchers RE, Gibson LJ, Hayes WC. Trabecular bone modulus and strength can depend on specimen geometry. J Biomech. 1993; 26:991–1000. [PubMed: 8349722]
85. Keaveny TM, Guo XE, Wachtel EF, McMahon TA, Hayes WC. Trabecular bone exhibits fully linear elastic behavior and yields at low strains. J Biomech. 1994; 27:1127–36. [PubMed: 7929462]

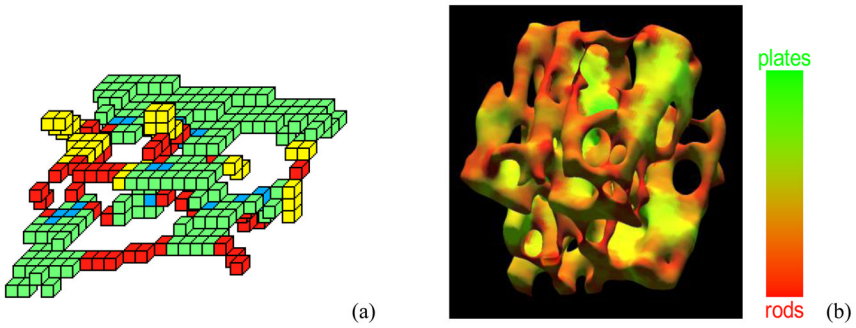

(a) (b)

Figure 1.

An illustrative comparison between DTA and VTA technologies. (a) A color-coded display of plates (green), rods (red), junctions (blue) and profiles (yellow) in a TB skeleton computed using DTA. (b) Classification of trabeculae on the continuum between perfect plates (green) and rod (red) using the proposed VTA method.

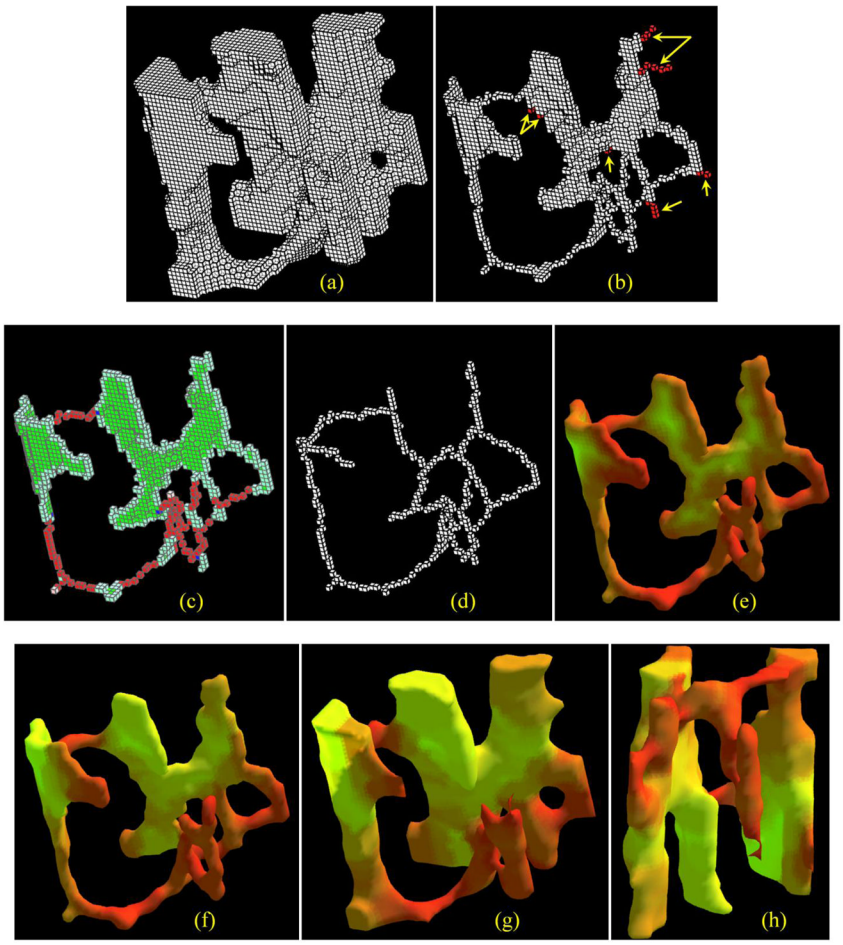

Figure 2.

Results of intermediate steps in VTA. (a) A TB region selected from μCT image of a human ankle specimen. (b) Results of skeletonization; noisy branches detected by pruning algorithm are colored in red. (c) Results of DTA indicating surface (green), surface-edge (light green), curve (red), curve-edge (pink), and junction (blue) voxels. (d) Results of arc skeletonization. (e–g) Color coded surface renditions of manifold distance transform (e), manifold scale (f) and volumetric topological analysis (g). (h) Same as (g) but from a different view.

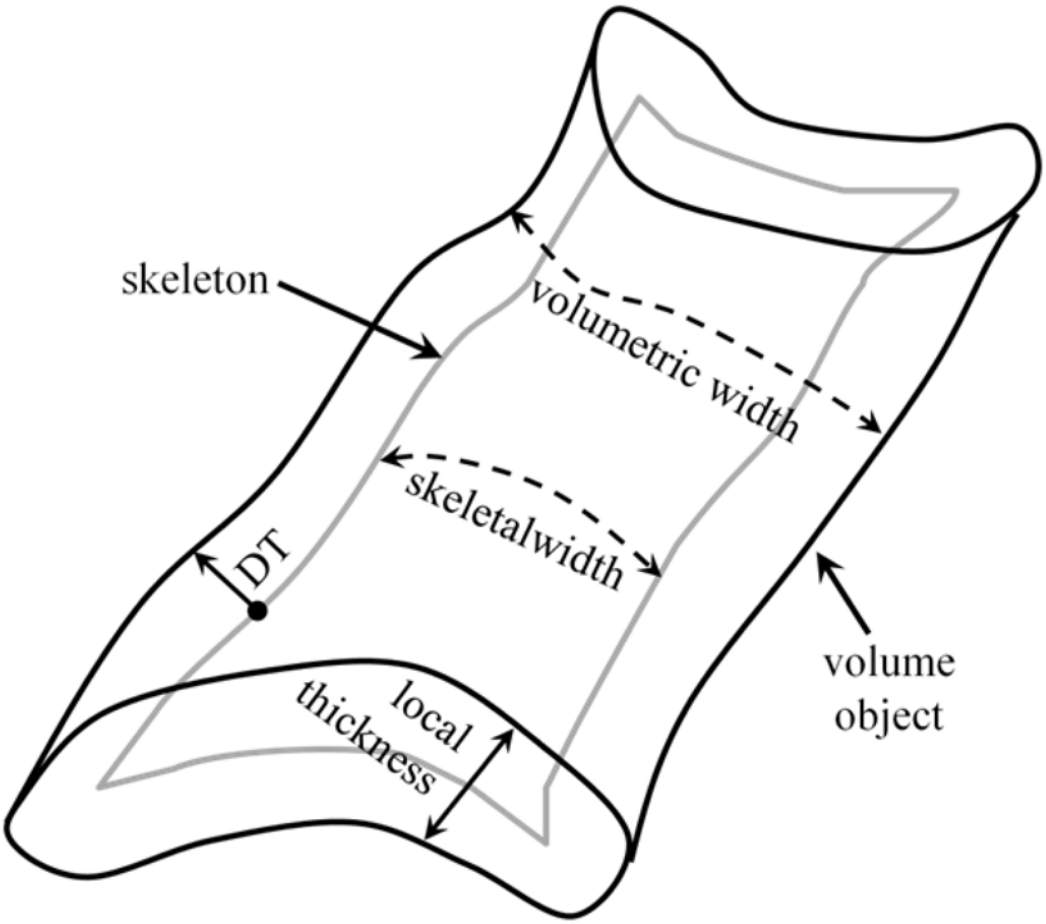

Figure 3.
An illustration of different measures on a surface-like volume objects and its skeleton. Local thickness may be computed by sampling binary or fuzzy distance transform values along skeletal locations. On the other hand, a technique similar to manifold distance transform (see Section 2.3) is needed to determine the width of an object. The difference between skeletal and volumetric widths is caused by iterative peeling technique used for skeletonization. This difference is alleviated by using an appropriate initialization of manifold distance transform at skeletal edges as discussed in Section 2.3.

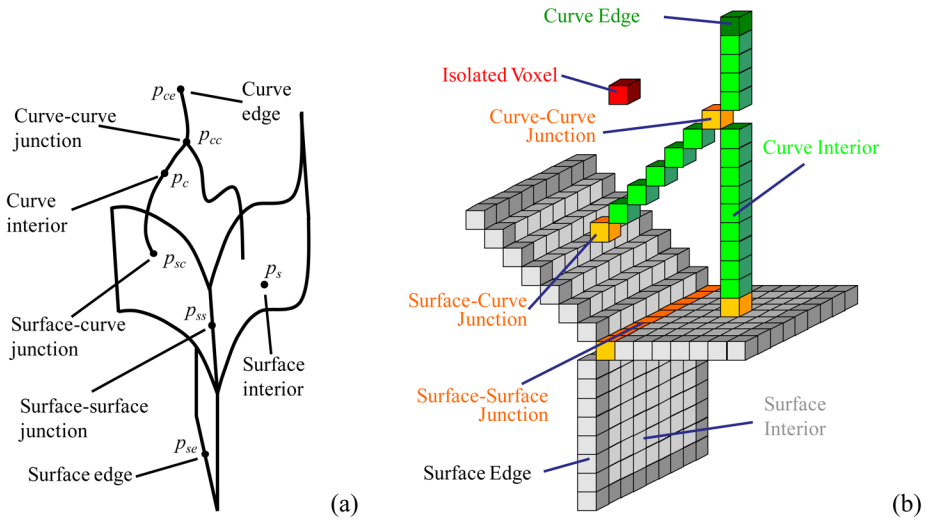

Figure 4.
Illustrations of possible topological classifications. (a) An example in the continuous 3D space. (b) An example in a digital space.

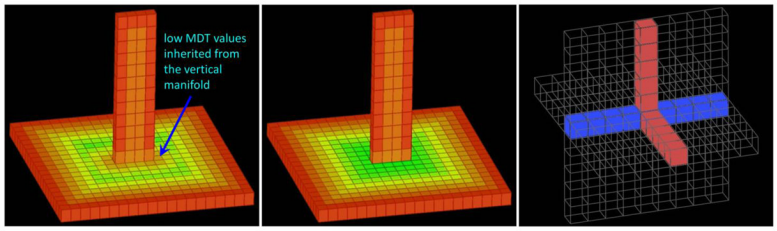

(a) (b) (c)

Figure 5.
(a) An illustration of MDT computed on a digital surface allowing MDT wave propagation paths to cross junctions. (b) Rectified MDT computation on the same digital surface. (c) An example of crossing between a 26-path (red) and a junction line (blue) on a (26,6) digital surface.

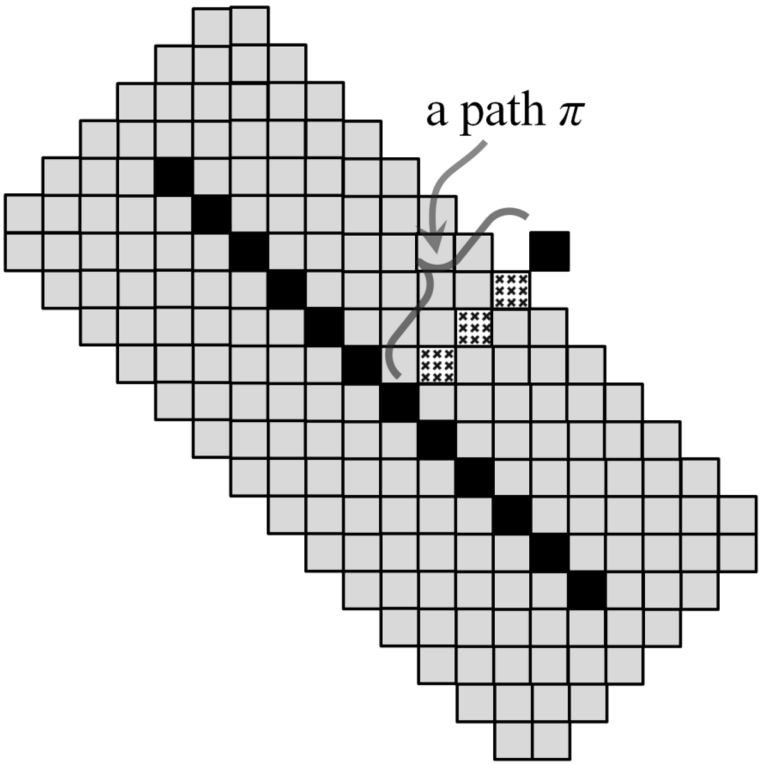

Figure 6.
An illustration of shape distance transform. Both black and textured pixels indicate skeletal pixels in the given shape. Black pixels survive in the skeletonization process as shape pixels, i.e., saved to preserve local shape of the structure. On the other hand textured pixels are preserved to maintain the topology. Shape distance only counts shape voxels on a path. For example, only one shape voxel contributes to the shape length of the path $\boldsymbol{\pi}$.

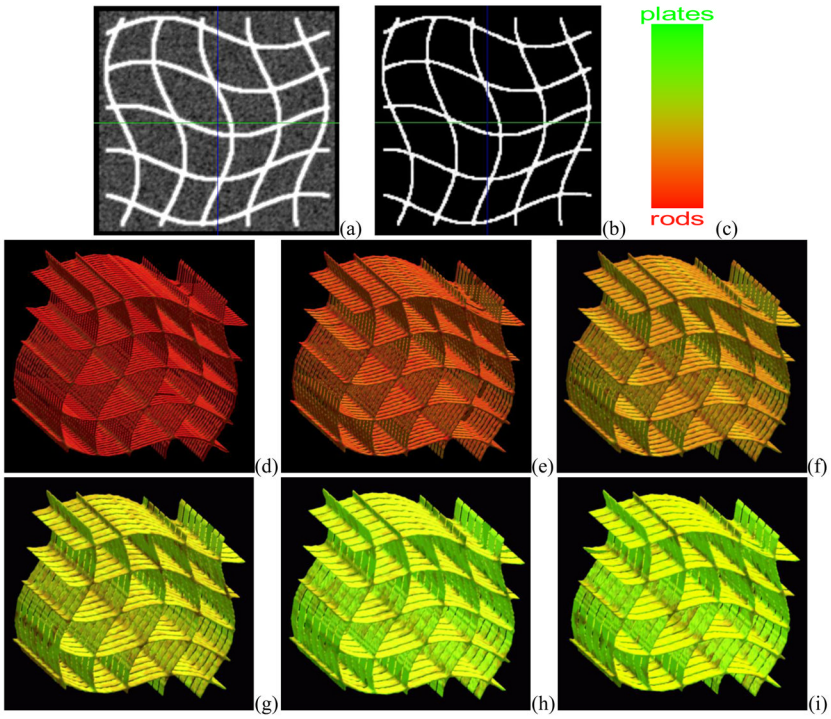

Figure 7.
Qualitative results of phantom analysis. (a,b) An image slice (a) and computed BVF map (b) from a phantom. (c) The commons color coding scheme used in (d–i). (d–i) VTA based classifications of plates and rods in different phantom images containing sinusoidal cross-plates at various widths.

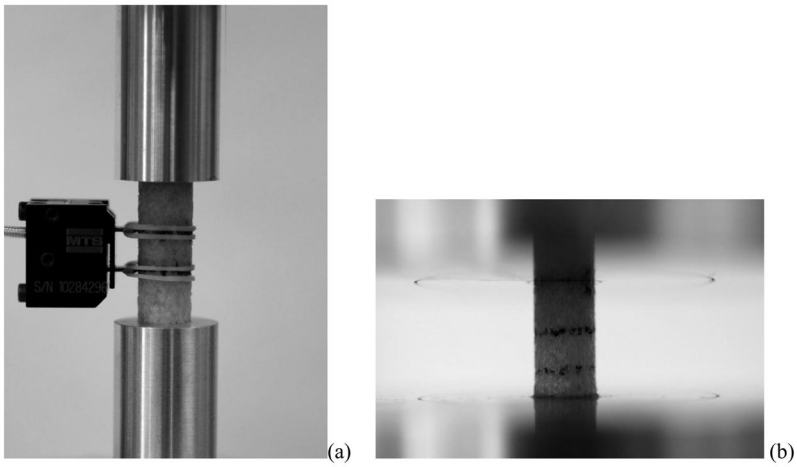

(a) (b)

Figure 8.
Compressive mechanical testing of TB specimens. (a) Extensometer testing. (b) Non-extensometer testing; note black lines indicating original extensometer position, with damaged bone removed from the bottom (proximal part) of the specimen.

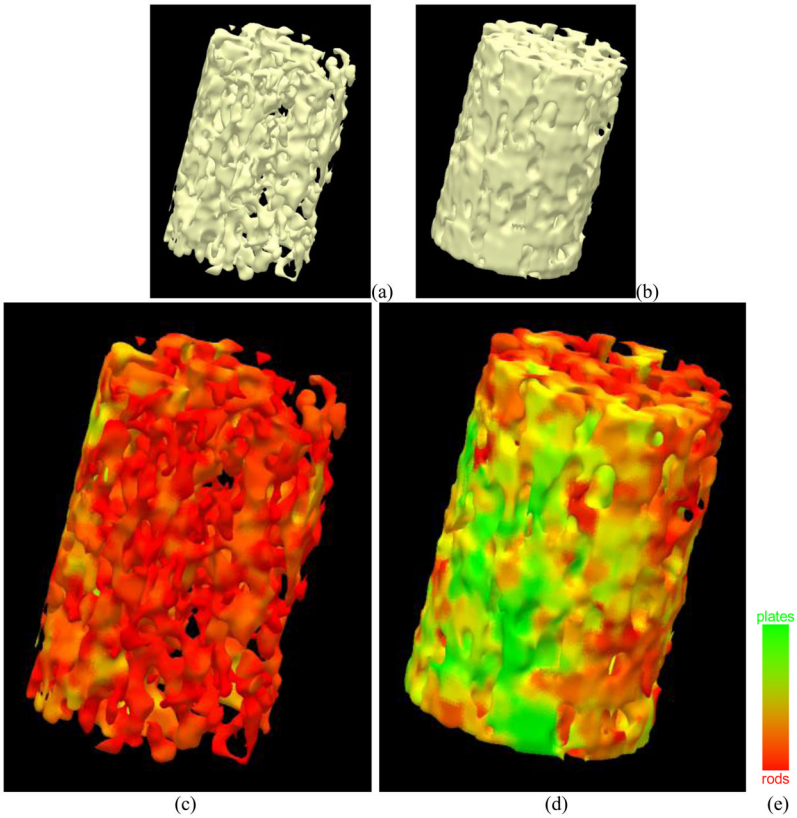

Figure 9.
Qualitative illustrations of the result of VTA classification on two TB specimens with distinctly different trabecular architecture. (a) A TB specimen with mostly rod-like trabeculae. (b) Another TB specimen with mostly plate-like trabeculae. (c,d) VTA based classifications of plates and rods of trabeculae in (a,b). (e) The commons color coding scheme used in (c,d).

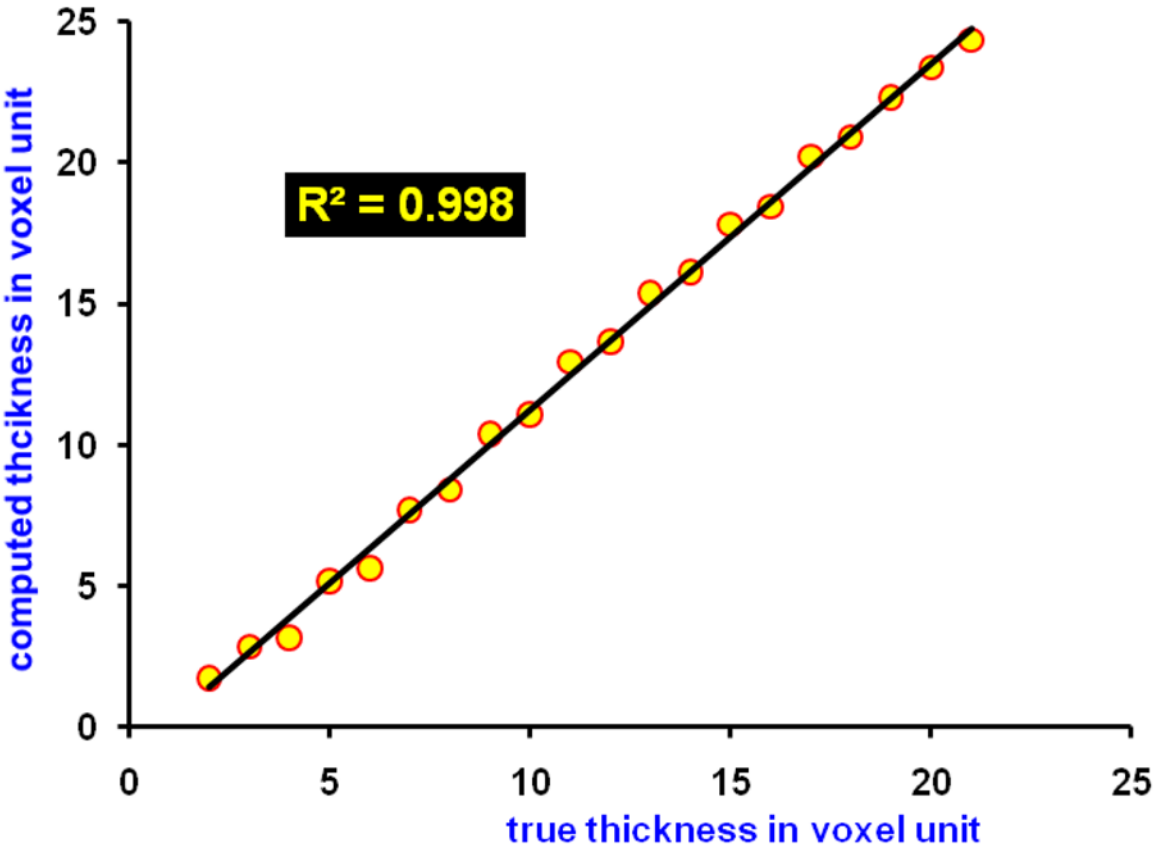

Figure 10.
Results of linear correlation analysis between true structure width and computed width using VTA method on computational phantoms illustrated in Figure 7.

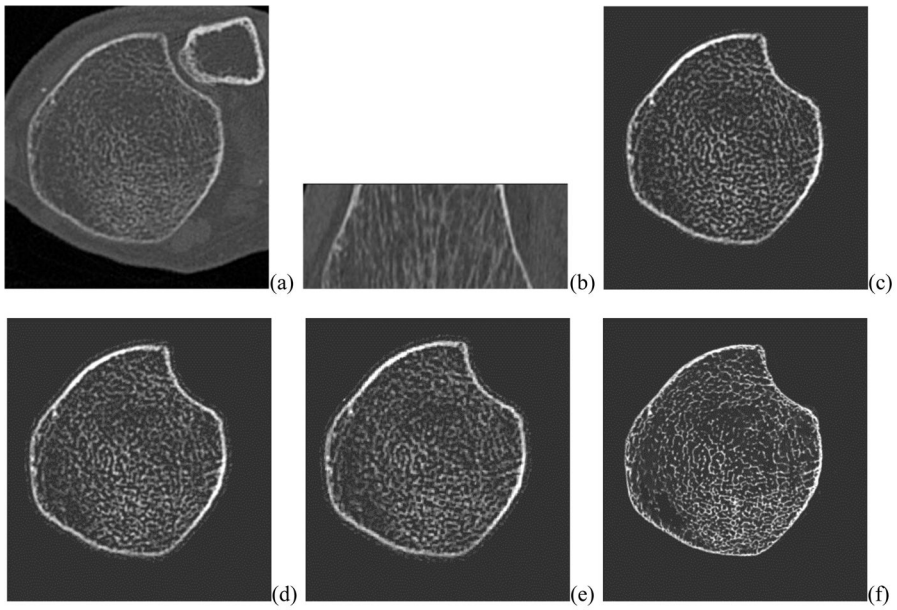

Figure 11.

A qualitative comparison of TB structures in repeat CT and μCT scans. (a,b) An axial and a coronal image slice from the first CT scan of distal tibia in a cadaveric ankle specimen. (c–f) A matching axial slice from post-registered BVF images of three repeat scans (c–e) and the single μCT scan (f).

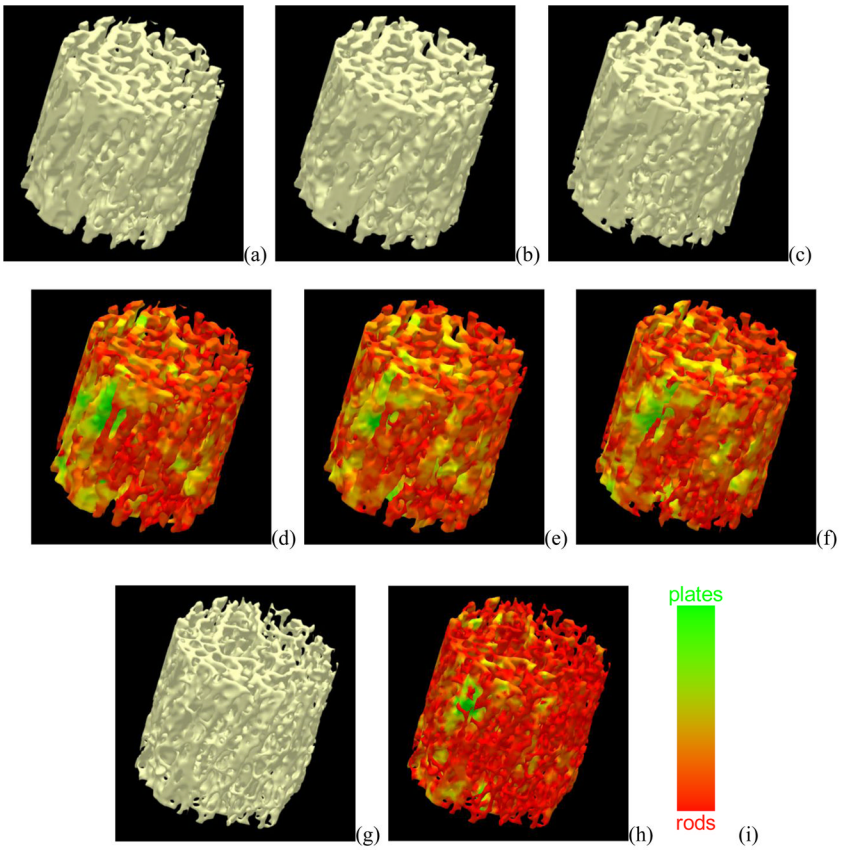

Figure 12.

Visual illustration of intra- and inter-modality reproducibility of VTA-based classification of TB. (a–c) Three dimensional renditions of TB over a matching VOI from post-registered repeat CT scans of a distal tibia specimen. (d–e) VTA-based classifications of three repeat scan TB data of (a–c). (g,h) Same as (a,d) but from the post-registered μCT data. (i) The common color coding bar used in (d–f, h).

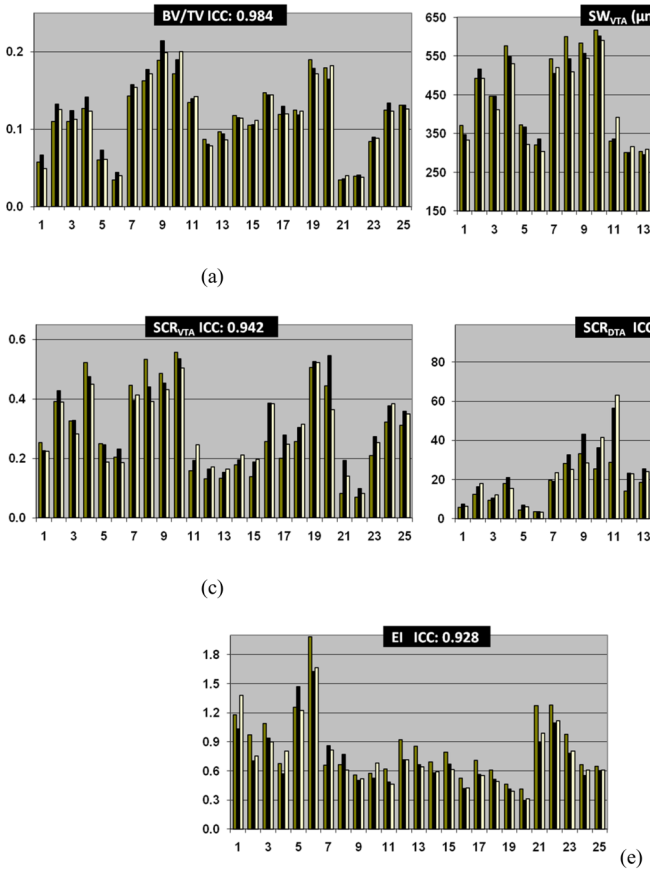

Figure 13.

Intra-modality reproducibility of different TB measures. (a–e) Intra-class correlation of different TB measures computed from matching VOIs in three repeat CT scans. Although, other TB measures are unit less, SW_{VTA} was computed in the unit of microns.

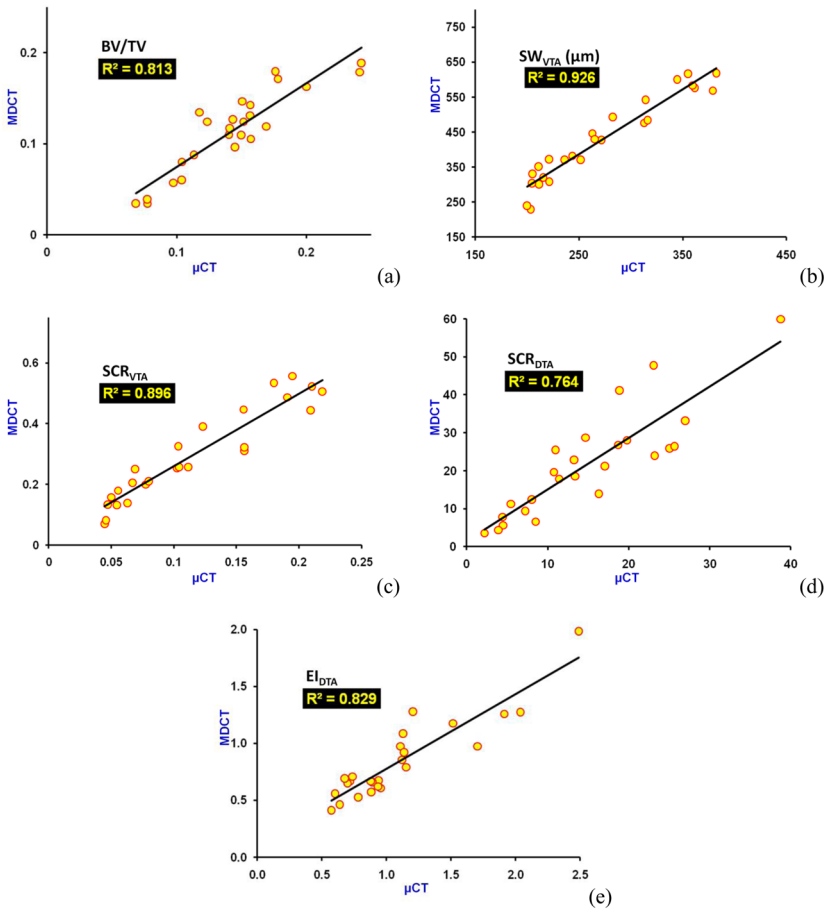

Figure 14.

Correlation of different TB measures computed via CT and μCT imaging. (a–e) Linear correlation of different TB measures computed from matching VOIs in CT and μCT images. Although, other TB measures are unit less, SW_{VTA} was computed in the unit of micronS.

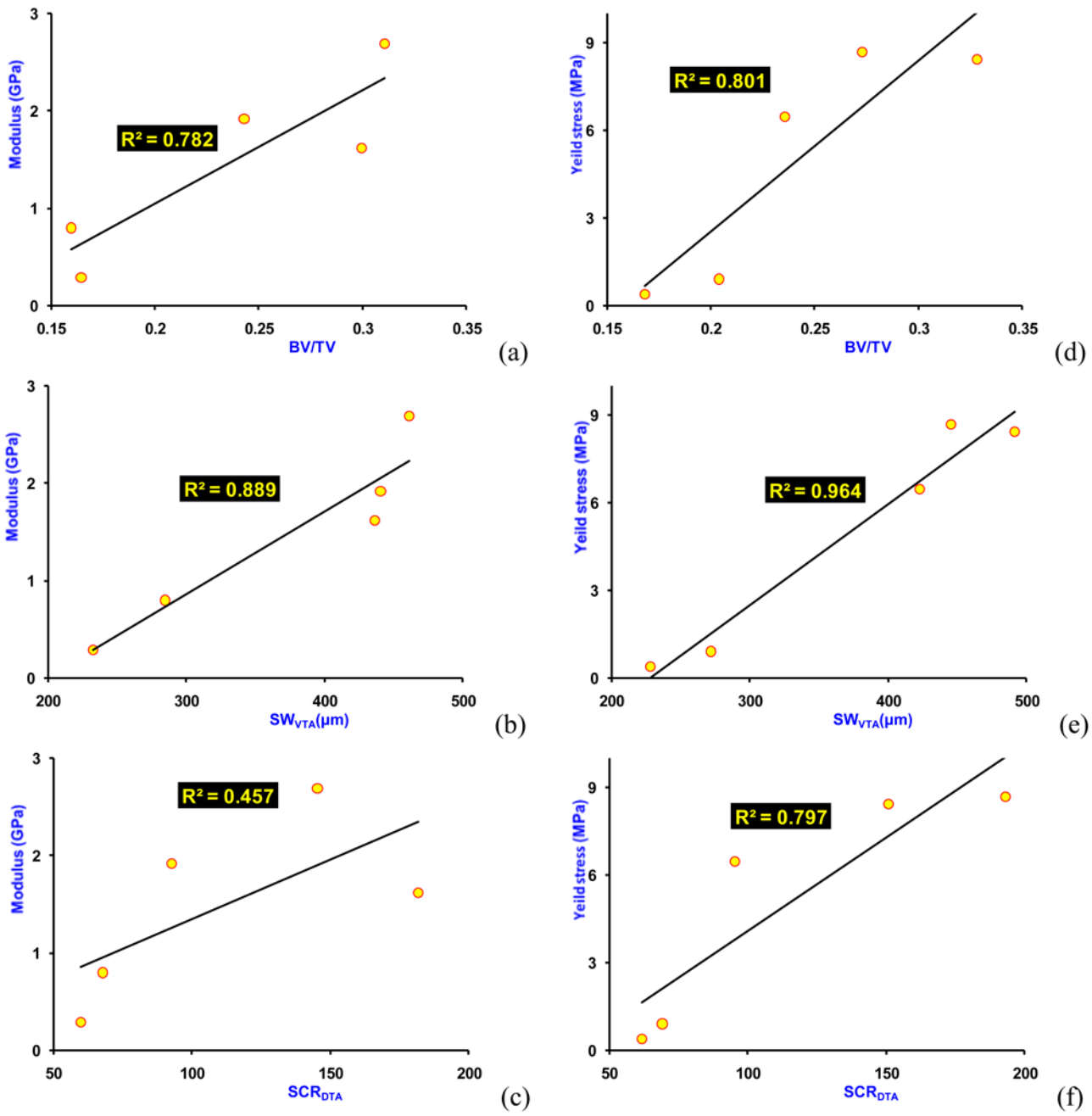

Figure 15.

Ability of different CT image-derived TB measures to predict TB s mechanical properties, with linear correlation (R^2 value) shown. Young's modulus vs. (a) BV/TV, (b) SW_{VTA} and (c) SCR_{DTA}. Yield stress vs. (d) BV/TV, (e) SW_{VTA} and (f) SCR_{DTA}.

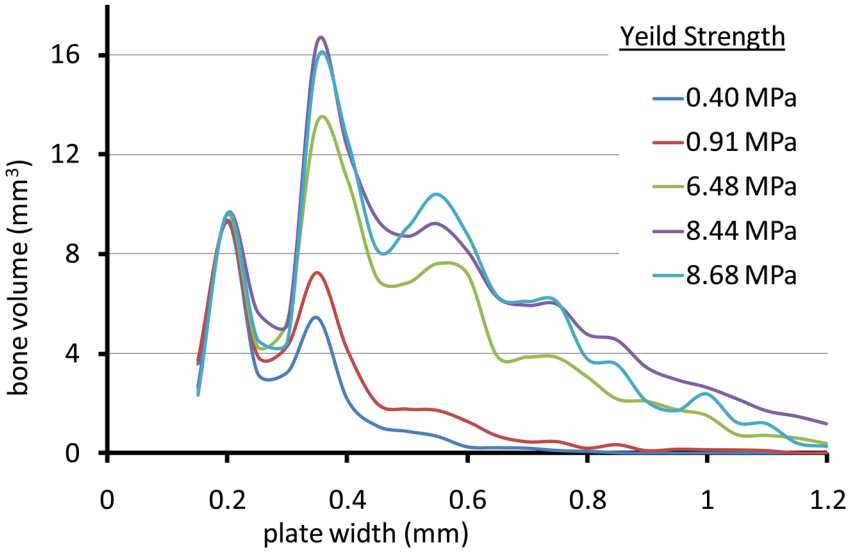

Figure 16.
Patterns of bone mass distributions at various plate widths for TB specimens with different measured mechanical strengths.

Table 1

Ability of different CT image-derived TB measures to predict TB s mechanical properties. Linear correlation (R^2 value) of different CT image-derived TB measures with (a) Young's modulus and (b) yield stress are listed.

(a)				
BV/TV	**SW_{VTA}**	**SCR_{VTA}**	**SCR_{DTA}**	**EI_{DTA}**
0.782	0.889	0.916	0.457	0.795

(b)				
BV/TV	**SW_{VTA}**	**SCR_{VTA}**	**SCR_{DTA}**	**EI_{DTA}**
0.801	0.964	0.954	0.797	0.898